Spectrochimica Acta Part A: Molecular and Biomolecular Spectroscopy 246 (2021) 118916

Contents lists available at ScienceDirect

Spectrochimica Acta Part A: Molecular and Biomolecular Spectroscopy

journal homepage: www.elsevier.com/locate/saa

Label-free screening of biochemical changes in macrophage-like cells following MoS_2 exposure using Raman micro-spectroscopy

Caroline Moore [a,*], Andrew Harvey [b], Jonathan N. Coleman [b], Hugh J. Byrne [a], Jennifer McIntyre [c]

[a] FOCAS Research Institute, Technological University Dublin, City Centre Campus, Dublin 8, Ireland
[b] Centre for Research on Adaptive Nanostructures & Nanodevices (CRANN) and Advanced Materials and BioEngineering Research (AMBER) Centre, Trinity College Dublin, Dublin 2, Ireland
[c] Department of Education, Trinity College Dublin, Dublin 2, Ireland

ARTICLE INFO

Article history:
Received 14 May 2020
Received in revised form 31 August 2020
Accepted 1 September 2020
Available online 16 September 2020

Keywords:
Molybdenum disulfide
Submicrometric plates
Raman micro-spectroscopy
Vesicle identification
Lipidic vesicles
Phosphatidyl lipids
Sphingomyelin
Cellular response

ABSTRACT

The emergence of large scale production techniques for 2D particulate materials has dramatically increased their applications potential. Understanding the interactions of biological cells with such particulate material is therefore of paramount importance, both for toxicological assessment and potential biomedical applications. Conventional in-vitro cytological assays commonly record only a single colorimetric end-point, and do not provide an in-depth analysis of how such materials are uptaken and processed within cells. To demonstrate its potential as an alternative, label free approach, confocal Raman micro-spectroscopy has been used to profile the cellular response of macrophage-like immune cells as a result of exposure to a sub-lethal dose of particulate MoS_2, as an example novel 2D material. Particles were seen to be uptaken and trafficked in sub-cellular vesicles, and this sensitive technique allows differences in the biochemical composition of the vesicles to be assessed and monitored as a function of time. Untreated macrophage-like cells contain lipidic vesicles which are found to be relatively rich in the membrane lipid sphingomyelin, key to the process of cell membrane regeneration. After exposure to MoS_2, the particulate material is seen to be invaginated in similar vesicles, the most prominent of which now, however, have spectroscopic signatures which are dominated by those of phosphatidyl family lipids, consistent with the phagocytotic pathway. The lipidic content of cells is seen to increase at all time-points (4, 24 and 72 h). although vesicles composed of sphingomyelin become more prominent again following a prolonged incubation of 72 h to a sub-lethal dose of MoS_2, as the immune cell has processed the particulate material and initiates recovery to a normal/untreated state. This study reveals Raman micro-spectroscopy is an effective method for monitoring cellular responses and evolution of organelle compositions in response to MoS_2 exposure. The additional benefit of using this technique is that cells can be monitored as a function of time, while it can also be used for screening other micro/nano materials for toxicology and/or establishing cell responses.

1. Introduction

Since the first concepts of nanotechnologies were mooted in 1959 by physicist Richard Feynman [1], the advances and interest in particulate material technology have grown immensely. Properties and characteristics of materials change when their sizes are reduced from three-dimensional (3D) bulk material to within the nanometer range. The isolation and characterisation of graphene monolayers, in 2004 [2], resulted in a surge in two-dimensional (2D) material research, due to the ever increasing range of potential applications. Graphene has shown promise in areas such as flexible electronic displays [3], sensors [4] and drug delivery [5]. The liquid phase exfoliation technique reported by Coleman et al. enabled the large scale production of high quality dispersed graphene for the first time [6], making the integration of particulate material in flexible devices, bio-sensors and/or medical applications more realistic in the foreseeable future. The process was demonstrated to be transferrable for use with other 2D layered materials such as Molybdenum disulphide (MoS_2) [7], commonly used in bulk form as an engine lubricant due to its low friction co-efficient [8]. MoS_2 has enhanced electronic properties on the nanometer scale [9] and has attracted growing attention due to its more favourable properties compared to its graphene analogue, based on its electronic band structure [10]. Single or few-layer MoS_2 nanometer or sub-micrometer scale particles have a direct band gap, giving them, for example, superior catalytic performance over their zero band gap equivalent [9,10].

Notably, measures have been taken to promote a more standardised nomenclature for 2D materials to reduce confusion and interpretation for both graphene and graphene related materials [11,12]. The international organisation of standardisation published a review article in 2015 regarding the terminology and definitions used in relation to particulate material in the field of nanotechnology [13]. Accordingly, a nanoparticle

* Corresponding author.
E-mail address: C10322785@mytudublin.ie (C. Moore).

https://doi.org/10.1016/j.saa.2020.118916
1386-1425/

is defined to be one in which all three dimensions are within the nanoscale range between 1 and 100 nm. A nanoplate is described as one in which only one dimension is within the nanometer range. The term nanosheet is used to indicate a single layer thickness. The materials used within this study contain few-layers of lateral dimension >100 nm, and therefore, the nomenclature used in this study is that of submicrometric plates.

Prior to 2D material translation into either industrial or medical arenas, assessment of the safety and potential risk of particulate materials is of paramount importance. Therefore, to prevent detrimental impacts on human health as a consequence of exposure to particulate material, understanding how such materials interact with biological cells is essential. In this context, macrophages play a critical role. Their role is to maintain homeostasis by removing foreign threats from circulation, amplifying an immune response and aiding in tissue repair [14,15]. Previously, a sub-lethal dose of 1 μg/ml MoS_2 submicron/nano plates was established for THP-1 monocytic cells differentiated to macrophages, by evaluating the effect of particulate exposure in terms of both cell viability and live/dead concentrations [16]. Notably, this concentration of particulate material resulted in no significant reduction of cell viability for THP-1 cells for 24, 48 or 72 h incubation time-points. Uptake of submicron/nanoplates following a 4 h incubation within the phagocytic macrophages was confirmed by both Transmission Electron Microscopy (TEM) and Raman micro-spectroscopy [16,17].

Whole cell Raman spectral mapping was previously employed to assess the capability of Raman micro-spectroscopy to identify material uptake in-vitro and to determine the fate and/or integrity of MoS_2 following phagocytosis [17]. It was observed that, following internalisation, particulate material was localised to discrete regions of the cell, the majority of vesicles being located within the cytoplasm in the peri-nuclear region. Degradation of MoS_2 plates in cells incubated for 24 h post-exposure could be observed, based on changes of the characteristic E^1_{2g} and A_{1g} features of MoS_2 [17,18]. A micro-environment rich in lipids from the phosphatidyl family was associated with material degradation, while non-degraded MoS_2 plates were encompassed within an environment rich in the enzyme lysozyme [17]. It was suggested that the lipopolysaccharide (LPS) contaminant on the surface of particulate material inhibited the activity of the enzyme, formally known as muramidase [19].

The previous cellular mapping study demonstrated the potential of Raman micro-spectroscopy to provide insight into the sub-cellular uptake, fate and/or degradation of MoS_2 submicron plates in individual THP-1 macrophages. It did not, however, explore the impact of cellular uptake, compared to untreated cells, and the characteristics of the phagocytotic process in the cell population as a whole. High spatial resolution mapping of individual cells to provide in-depth information in the form of pseudo colour images created based on spectral information [20,21] can take anything between minutes to hours to complete [20,22], however, depending on the laser spot, step size and desired quality of signal, and, as a result, only a small proportion of the cell population is typically analysed [23]. Therefore, to examine the metabolic response of the cell population following internalisation of MoS_2, rather than exhaustively mapping each cell, point spectra were recorded for discrete regions of multiple cells, enabling a larger population response to be established. As a result, prominent lipidic vesicles, which were previously identified as being involved in the catabolisation of particulate material, were selected to gain insight into the cellular response following exposure to MoS_2. Notably, whereas the analysis of the previous study specifically targeted MoS_2 containing vesicles in individual treated cells [17], using Raman point spectral analysis to sampling vesicles in multiple untreated and treated cells, in an unsupervised fashion, this study aims to further understand the response of the immune cell population following interactions with MoS_2 and further identify any biochemical alterations between untreated cells and those exposed to the MoS_2. The same pulse chase exposure method was applied for this study, whereby cells were incubated for 4 (T4), 24 (T24) and 72 h (T72) subsequent to an initial exposure of 4 h to 1 μg/ml MoS_2 submicron/nano plates.

2. Materials and methods

2.1. 2D MoS_2 production

MoS_2 powder (Sigma Aldrich, Ireland) was dispersed in aqueous sodium cholate (SC) surfactant (6 g/l) and sonicated for 1 h before subsequently centrifuging at 5 kprm (2660 g) for 90 min to remove sample impurities found in the supernatant. The sedimented particulate material was re-dispersed in freshly prepared SC (0.5 g/l) and sonicated for a further 6 h. This stock solution was then prepared by Liquid Cascade Centrifugation (LCC), by which samples are subjected to a range of centrifugal steps using different filter sizes to produce stable plates of a predetermined size [24]. A detailed description of the LCC protocol has been previously published [24]. The degree of stability of MoS2 plates in surfactant over time is indicated by a Zeta potential of −40 mV [25]. The lateral size and layer number of MoS2 plates was determined using UV–Vis spectroscopy to be 120 ± 20 nm and 3–5 layers, respectively [26].

2.2. Cell culture

Human acute monocytic leukemia (THP-1) cells were cultured in Roswell Park Memorial Institute (RPMI) medium (Gibco, Bio-sciences Ltd., Ireland). RPMI was supplemented with 10% Foetal Bovine Serum (FBS). Cells were maintained in a humidified atmosphere at 37 °C and 5% CO_2. THP-1 monocytic cells were seeded onto calcium fluoride (CaF_2) discs (Crystan, United Kingdom) at a concentration of 1×10^5 cell/ml (3 ml/sample) in 6-well culture plates and differentiated into macrophage-like cells by incubating them with 100 nM phorbol 12-myristate 13-acetate (PMA) for 72 h [27].

2.3. Cellular preparation for Raman micro-spectroscopy

To ensure the acquisition of high-quality spectra, sample preparation and measurement conditions were optimised. Subsequent to optimisation of the Raman protocol, THP-1 cells were exposed to MoS_2 for 4 h, to allow sufficient time for internalisation, and then cells were incubated in supplemented medium (no MoS_2 present) for a specified amount of time (4, 24 and 72 h). Subsequent to PMA differentiation, untreated cells were incubated in supplemented media containing no MoS_2 for the duration of the experiment (72 h). Cells were seeded within a 6-well plate and samples were prepared in chronological stages so that all incubation time-points were synchronised to finish at the same time. Following incubation, cells were washed twice with pre-warmed phosphate buffer saline (PBS) and fixed in 4% formalin (3 ml/sample) for 15–20 min at room temperature [28]. Subsequent to fixation, cells were washed twice with Millipore water and left in water for Raman spectroscopic analysis.

2.4. Raman spectroscopy of THP-1 cells

Raman spectra were recorded using a Horiba Jobin-Yvon LabRAM HR800 spectrometer equipped with a 532 nm solid state diode laser (50 mW), with a single edge filter and 600 g/mm line grating. Raman measurements for this study were performed using the upright microscope. All measurements were acquired in water with a 100× water immersion objective (numerical aperture 0.9, LUMPlanF1, Olympus), producing a focal spot size of ~1 μm. Raman point spectra were recorded over a spectral range from 300 to 3900 cm^{-1}. Spectra were recorded in 15 s acquisitions and 2 accumulations, for 40 cells at each time-point. The CaF_2 substrate has minimal background contribution of only a distinct band at 321 cm^{-1}, which does not overlap with MoS_2 or cellular

information [29]. Spectra were obtained from both peri-nuclear vesicles and nuclear areas of the cell.

2.5. Pre-processing analysis of Raman spectra

Subsequent to Raman acquisition, data was analysed and pre-processed in Matlab (MathWorks, Ireland) using in-house scripts. Data was smoothed with a Savitzky-Golay filter (order = 3, window = 9) and spectra were separated for analysis into two sub-groups (lower wavenumber (LWN) and higher wavenumber (HWN)) for further pre-processing and data analysis. For the LWN range, spectra were cut from 800 to 1800 cm^{-1} and background corrected using Extended Multiplicative Scatter Correction (EMSC) [30]. To carry out EMSC, a cell reference spectrum along with a pure spectrum of water (background) must be input. The EMSC algorithm then functions by applying a weighted sum of the background to be removed accompanied by a polynomial baseline correction to remove the water from the dataset. Outliers were removed and datasets were vector normalised prior to principal component analysis (PCA). For the HWN region, backgrounds were corrected using EMSC, spectral range cut to 2700–3100 cm^{-1}, outliers removed and vector normalised prior to PCA. PCA is a data processing technique commonly utilised to discriminate different samples based on variations in their Raman spectroscopic profiles, which ultimately correspond to differences in biochemical composition [31]. The spectral features discriminating the two or more data sets are then displayed as principal component (PC) loadings. The highest degree of variability is displayed by PC1, which decreases in subsequent PCs.

A one-way ANOVA was used to determine the significance of separation in clusters following PCA by analysing the variance between the mean of different groups.

For further identification of spectral contributions, an in-house dataset of spectra of 82 standards was used. A weighted spectrum was calculated by subtracting one standard (phosphatidyl – negative) from another (sphingomyelin – positive) and then directly compared with the PC loadings.

2.6. Oil Red O lipid quantification

THP-1 cells were seeded at a concentration of 1×10^5 cell/ml (3 ml/sample) in 6-well culture plates and differentiated into macrophage-like cells by incubating them with 100 nM phorbol 12-myristate 13-acetate (PMA) for 72 h. Following incubation with MoS_2 and incubation for a specific amount of time (4, 24 and 72 h), the cells were washed and fixed, as described in Cellular Preparation for Raman micro-spectroscopy above, and the samples were allowed to air-dry overnight prior to staining. Oil red O staining was prepared fresh and filtered before staining the cells for 15 min at room temperature (3 ml/sample). Oil red O was removed, and samples were washed three times with distilled water. Samples were incubated in isopropanol for 15–20 min on a plate rocker. Subsequently, 200 μl of eluted dye was removed and transferred to 96-well plates and the absorbance recorded at 540 nm using a SpectraMax plate reader (Molecular Devices, USA).

3. Results

3.1. Morphology and lipidic content of untreated THP-1 cells and those exposed to MoS_2

After differentiation of monocytic suspension cells to adherent macrophage-like cells, by incubation with PMA, THP-1 cells are seen to be rich in subcellular vesicles, predominantly localised in the peri-nuclear region, as shown in the white light image of Fig. 1A(i). It is well known that vesicles play an essential role in the process of membrane maintenance, exo/endocytosis and are commonly found in the peri-nuclear cloud surrounding the nucleus [32,33]. When cells have been incubated for 4 h post-exposure to MoS_2, they become difficult to image, and the subcellular content is not as clearly defined, as shown in Fig. 1A(ii). When macrophages are exposed to a foreign material, they initiate the process of phagocytosis. This involves morphological changes and cytoskeleton rearrangements to form pseudopodial extension which surround the material prior to internalisation within phagocytic vesicles [15]. As macrophages are in the early stages of reacting to MoS_2 within their environment following a 4 h incubation, cells were observed to be rounder in shape and therefore vesicles were compacted and difficult to visualise in the same plane as the nucleus. As can be seen in Fig. 1A(iii–iv), when cells have been incubated for an extended time period of 24 or 72 h following exposure to MoS_2, the cells are more easily imaged, as they have become more spread out across the bottom of the plate, and subcellular vesicles can be easily visualised. The lipidic content of untreated (NT) THP-1 cell cultures and those exposed to MoS_2 and incubated over time (T4, T24, T24), was quantified by the use of Oil Red O staining, as described in the Materials and Methods Section 2, and can be seen in Fig. 1B, in which an increase in lipid content can be observed as an increased Oil Red O absorbance at all time-points, when compared to untreated cells. The highest level of lipid content was observed in the cell cultures incubated for 24 h post-exposure to MoS_2, which is followed by a decrease following a prolonged incubation of 72 h. Previously, a similar trend in lipidic content was observed by brightfield images of both exposed and untreated THP-1 cells subsequent to Oil Red O staining [17]. Notably, the images of THP-1 cells incubated for 24 h post exposure to MoS_2 revealed a significant amount of lipids external to the cells [17], and therefore the recorded lipidic content is not exclusively intracellular. To further evaluate the cellular response to MoS_2 exposure, Raman point spectra were recorded for these lipidic vesicles for both untreated THP-1 cells and those exposed to MoS_2 and monitored as a function of time, post exposure (T4, T24 and T72).

3.2. Raman point spectra analysis to identify any biochemical changes in THP-1 cells incubated for 4 h post-exposure to MoS_2

Raman micro-spectroscopy has been used to identify the differences between untreated THP-1 cells (NT), incubated in supplemented medium, and those which have been similarly incubated for 4 h (T4), 24 h (T24) and 72 h (T72) following exposure to MoS_2 (1 μg/ml) for 4 h. Any changes or alterations in the cellular biochemical composition can aid in understanding the effect of exposure to the submicron plates. Notably, when using a 532 nm laser source, first and second order Raman bands for MoS_2 are resonantly enhanced in the region ~300–800 cm^{-1} [34,35]. Therefore, a range of 800–1800 cm^{-1} was used to ensure no interference from particulate material when interpreting the biological spectral signature. Analysis of point spectra taken from peri-nuclear vesicles, in the range of 800–1800 cm^{-1}, can be seen in Fig. 2A (i–iii). Pre-processed spectra of NT (red) and T4 (blue) have been plotted and are displayed in Fig. 2A(i), in which subtle but visible differences have been highlighted within the shaded areas. The associated bands can be generically assigned according to literature [36–39] and are detailed in Table 1. PCA was then carried out to better compare NT and T4, as shown in the scatter plot in Fig. 2A(ii), in which NT (red) is differentiated from T4 (blue) based on PC1. The loadings for PC1 are displayed in Fig. 2A(iii), better highlighting the discriminating peaks, which indicates that NT contains relatively large amounts of lipids (1061, 1128, 1296, 1437–1440, 1464 and 1743 cm^{-1}) along with carbohydrates (888 and 1128 cm^{-1}). Discriminating features of cells incubated for 4 h following exposure to MoS_2 are represented by negative peaks, also indicating the relative prominence of lipidic components (866, 974, 1267 and 1660–1665 cm^{-1}). The prominence of lipids in the PC loading is consistent with vesicles originating from the plasma membrane, as well as vesicles which take part in endo/exocytosis pathways [32]. Therefore, NT and T4 vesicles have been confirmed as lipidic based on PCA although more detailed analysis will be conducted in the following section to further identify which lipids are

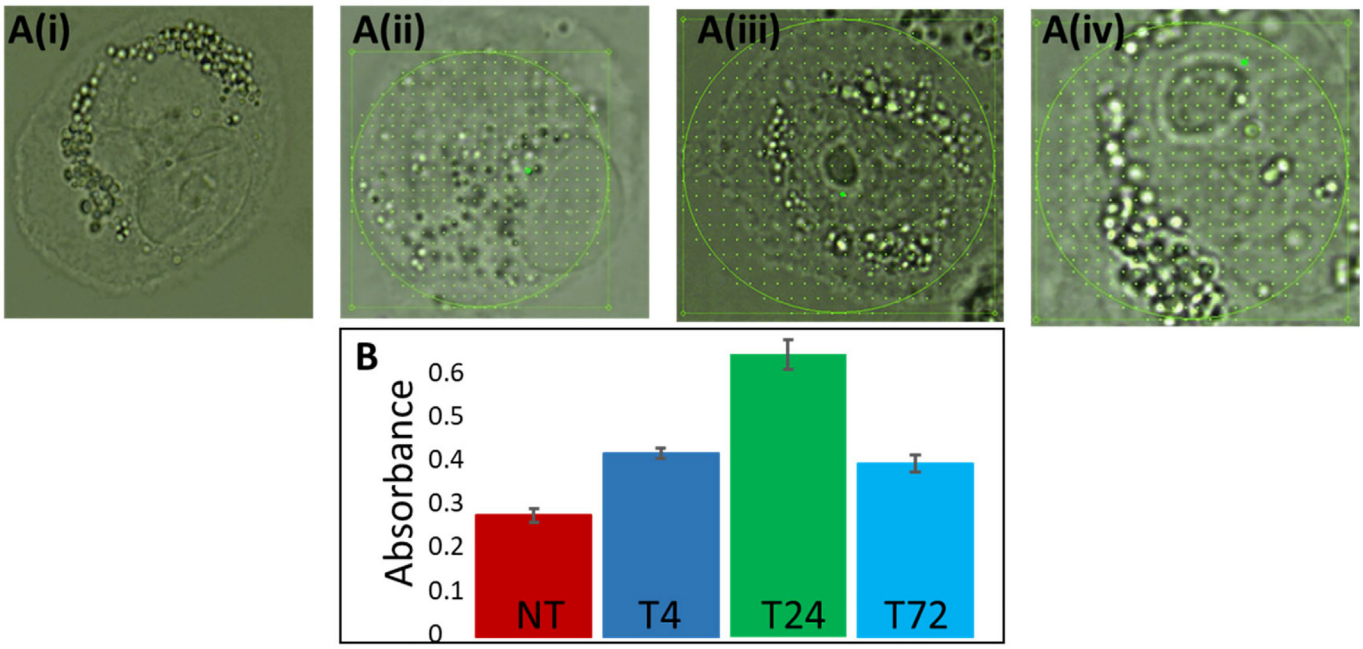

Fig. 1. White light images of differentiated THP-1 cells panel A(i) untreated cells, A(ii) 4 h incubation, A(iii) 24 h incubation and A(iv) 72 h incubation following treatment with MoS_2 for 4 h to allow internalisation. Panel B illustrates the quantification of hydrophobic lipids present in THP-1 cells in all treatment conditions by the use of Oil Red O staining. (Error bars display standard deviation).

discriminating factors for vesicles in NT compared to those of cells which have been exposed to MoS_2. Employing a one-way ANOVA test to analyse the variance between the two independent test groups to determine the significance of cluster separation, a p value of $<10^{-9}$ was obtained for NT versus T4 for both LWN (4.6×10^{-9}) and HWN (4.9×10^{-11}) regions, indicating significant separation.

Similar to the analysis in Fig. 2A, PCA was applied to the point spectra from NT and T4 datasets to identify any spectral differences in the range of 2700–3100 cm^{-1}, the results of which are shown in Fig. 2B(i–iii). In this case, pre-processed spectra of NT and T4 are displayed in Fig. 2B (i). NT responses are clearly differentiated from those of T4 based on PC2. The loadings for PC2 are displayed in Fig. 2B(iii), which shows NT is relatively rich in protein and lipids (2844, 2883, 2981–2991 cm^{-1}). Similar to the LWN region, PC loadings representing cells from the T4 dataset are also dominated by lipidic peaks (2854 and 3015 cm^{-1}), which will be further investigated for lipid identification in the following section.

3.3. Lipid identification

In PCA, the loadings represent the differences between the vesicular composition of NT cells and those that have been exposed to particulate material. Generic assignments can be made based on literature, according to general classes of biomolecules, such as lipids, proteins, DNA/RNA and more [36–39]. However, there are many different forms of lipids, each with a different spectral signature which may contribute to differentiating the Raman signatures of the NT and T4 cell populations.

Based on an in house dataset of 82 pure biological macromolecule components including, but not limited to, proteins, lipids, and enzymes, the assignment of featured bands listed in Table 1 can be further identified. From all the components tested, positive PC loadings representing untreated cells showed a profile consistent with that of a lipid called sphingomyelin (SM), the Raman spectrum of which is shown in Fig. 3A(i) (LWN) and 3A(ii) (HWN). This membrane lipid is composed of N-acyl-sphingosine (ceramide) bound to very long chain fatty acids and phosphocholine. SM synthase functions by combining both ceramide and phosphocholine head groups to form SM. Both phosphatidylcholine (PPC) and phosphatidylethanolamine (PPE) are found in abundance following differentiation of monocytes into macrophages [40]. Notably, phosphocholine, used in SM synthesis, is derived from phosphatidylcholine.

Negative peaks in the PC loadings which represent vesicles from THP-1 cells exposed to MoS_2 were also compared with the in-house dataset and a high degree of similarity with the phosphatidyl family lipids was observed (Fig. 3B(i) (LWN) and 3B(ii) (HWN)). Phosphatidyl lipids contain an acyl group derived from a phosphatic acid and are commonly detected in cell membranes with the addition of esterified head groups such as choline, ethanolamine, serine etc. [41]. A difference spectrum was created by a weighted subtraction of one component (phosphatidyl – Fig. 3B(i–ii)) from the other (sphingomyelin - Fig. 3A (i–ii)), which is then compared to the PC loadings (Fig. 3C(i–ii)). Although the match is not exact, as may be expected due to the multitude of other contributing species, most of the main features of the PC loadings are reproduced in the difference spectrum, in both the LWN and HWN regions.

Therefore, although NT and T4 datasets were both identified as generically lipidic in Fig. 2, it is now confirmed that the different specific biochemical compositions of each dataset could be identified with Raman micro-spectroscopy based on their different lipidic profiles. Notably, results show the robustness and advantages of using Raman micro-spectroscopy for providing detailed information from within the same spectra as the same lipids were identified for PC loadings for both the LWN (Fig. 3A(iii)) and HWN (Fig. 3BB(iii)) regions for untreated cells and those incubated for 4 h following exposure to MoS_2. Previously, Raman spectral maps were recorded for THP-1 cells exposed to MoS_2 using a similar pulse chase exposure method. The material micro-environment was characterised and similarly associated with members of the phosphatidyl family [17] further confirming the strength and reliability of Raman micro-spectroscopy to reveal the sub-cellular response of the cells to the MoS_2. Additionally, it should be noted, that the increase in lipid content witnessed in T4 cells (Fig. 1B) as a result MoS_2 exposure may mean the likelihood of sampling vesicles rich in phosphatidyl lipids more dominant than the intrinsic SM detected in NT cells.

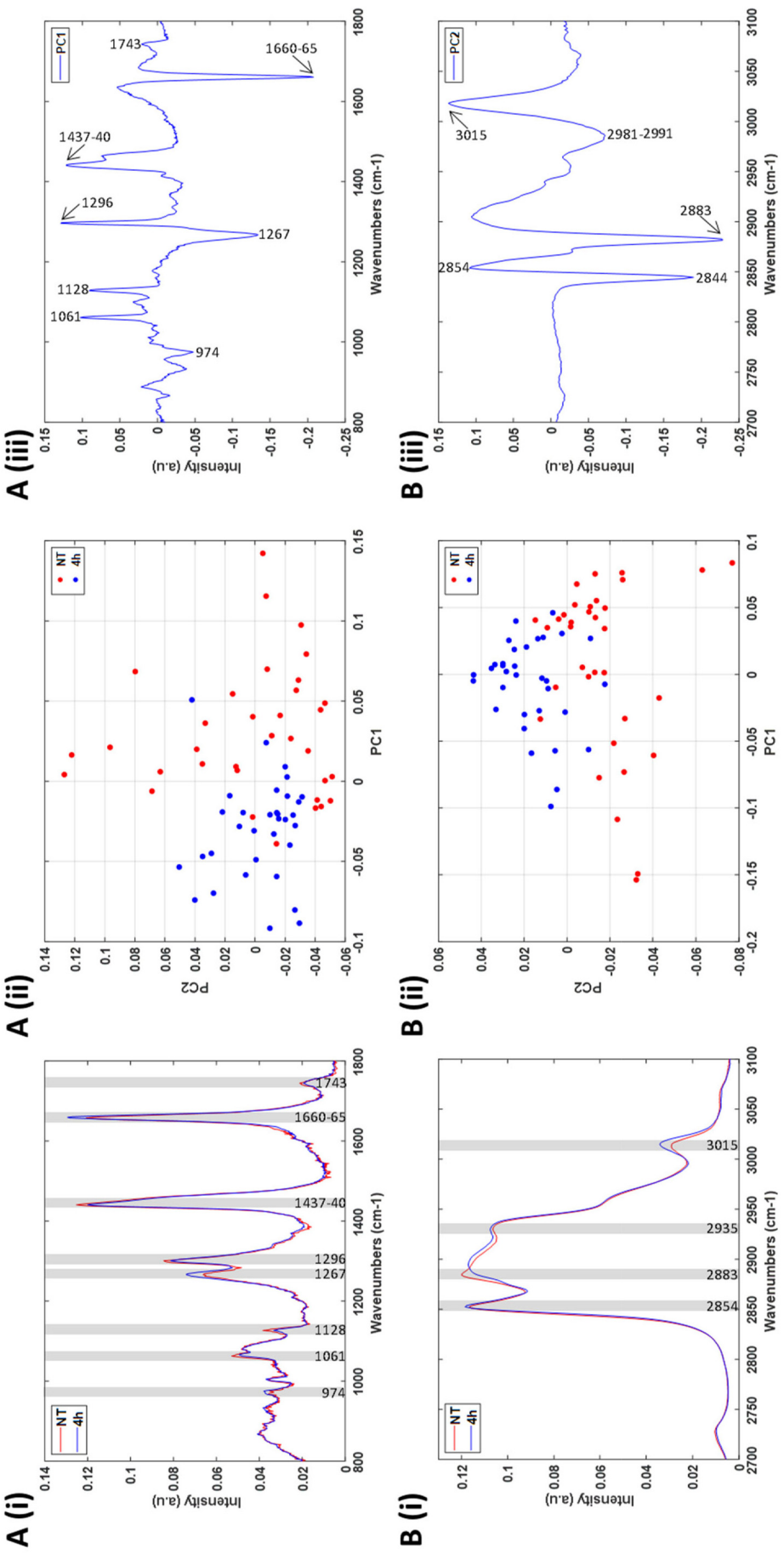

Fig. 2. Raman micro-spectroscopic and Principal components analysis to investigate differences between untreated THP-1 cells and cells incubated for 4 h following exposure to MoS_2. Panel A(i) pre-processed spectra of NT (red) and 4 h (Blue) in the range of 800–1800 cm^{-1}. Panel A(ii) PCA scatter plot of Raman spectra from untreated cells (NT, red) and cells incubated for 4 h (blue) in the range of 800–1800 cm^{-1}, plotted PC1 versus PC2. Panel A(iii) PC1 loadings demonstrating the spectral differences in the range of 800–1800 cm^{-1}. Panel B(i) pre-processed spectra of NT (red) and 4 h (Blue) in the range of 2700–3100 cm^{-1}. Panel B(ii) PCA scatter plot of Raman spectra from NT and cells incubated for 4 h in the range of 2700–3100 cm^{-1}, plotted PC1 versus PC2. Panel B(iii) PC2 loadings demonstrating the spectral differences in the range of 2700–3100 cm^{-1}.

Table 1
Band assignments [36–39] related to differences detected between untreated THP-1 cells and those that have been exposed to MoS_2 and incubated for 4 h (T4).

Raman peaks (cm^{-1})	Untreated (NT)	Treated (4 h)	Vibration & functional groups
866		Lipid	O-C-C-N Symmetric stretch
888	Carbohydrates		C-C stretch
974		Lipid	=CH Bending
1061	Lipid		C-C stretch
1128	Carbohydrates		C-O stretch
	Lipid		C—C acyl backbone
1267		Lipid	=C-H in-plane hydrogen bending
1296	Lipid		CH_2 deformation
1437–1440	Lipid		CH_2 deformation
1660–1665		Lipid	C=C stretch
1743	Lipid		C=O carbonyl stretch
2844	Lipid		CH_2 symmetric stretch
2854		Lipid	Aliphatic lipid CH stretch vibration
2883	Lipid		CH_2 asymmetric stretch
2981–2991	Lipid		CH stretch
3015		Lipid	=C-H

3.4. Raman point spectra analysis to identify any biochemical changes in THP-1 cells incubated for 24 h post-exposure to MoS_2

The next step was to compare untreated cells to those that have been incubated for a longer time period of 24 h post-exposure to MoS_2. Separation based on PC1 in the spectral range of 800–1800 cm^{-1} is displayed in Fig. 4A(ii). The features of the differentiating principal component (Fig. 4A(iii)) are almost identical to the loading for NT versus T4 (Fig. 2A(iii)), with the exception of minor differences in the lipidic peak positioned at 1464 cm^{-1}, which has previously been reported as CH_2/CH_3 deformations in cholesterol and triacylglycerols [42]. Notably, a broader distribution of data points can be observed in cells incubated for 24 h, in that a small proportion of datapoints has a clear overlap with untreated cells. Similarly, NT and T24 datasets were analysed in the HWN range of 2700–3100 cm^{-1}, as can be seen in Fig. 4B(i–iii). Separation based on PC2 can also be observed for NT versus T24 post-exposure to MoS_2 (Fig. 4B(ii)). Notably, a similar mixed population of T24 cells is identified in the HWN region. The separating components observed for both the LWN and HWN (Fig. 4B(iii)) regions are similar to trends observed for NT versus T4 in Fig. 2. This suggests that macrophages incubated for either 4 or 24 h following exposure to MoS_2 have a similar cellular response, in the form of sub-cellular vesicles of similar biochemical composition, which are predominantly constituted by lipids of the phosphatidyl family. Additionally, a saturation in lipid content was detected for T24 cells (Fig. 1B) as a result MoS_2 exposure and therefore the likelihood of randomly sampling vesicles rich in phosphatidyl lipids more likely than the intrinsic SM detected in NT cells. When a one-way ANOVA was performed, while a p value of 6.9×10^{-8} was obtained for NT versus T24 for the HWN region, a value of 2×10^{-4} was obtained for the LWN region, indicating a lesser degree of separation than observed for 4 h.

3.5. Raman point spectra analysis to identify any biochemical changes in THP-1 cells incubated for 72 h post-exposure to MoS_2

PCA of NT (red) cells versus T72 (cyan) can be seen in Fig. 5A(ii), in which a degree of separation is achieved, although a high degree of overlap of datapoints is observed, suggesting a similar biochemical composition between the two datasets in the spectral range of 800–1800 cm^{-1}. The differentiating spectral features, represented by PC1 (Fig. 5A(iii)), show NT to be relatively rich in carbohydrates (888 and 1128 cm^{-1}) along with lipids (1061, 1128, 1297 and 1437 cm^{-1}), consistent with the peaks observed in previous figures (Figs. 2 and 4), further confirming the presence of SM in NT samples. T72 samples are generally positioned on the positive side of PC1, indicating the prominence of lipids (933, 1267 and 1660–1665 cm^{-1}), which have been previously identified as members of the phosphatidyl family. These peaks were also identified in both T4 and T24 vesicles, although a broader distribution can be seen in T72 cells. No well-defined sub-populations can be detected in T72, although the overlap with NT cells appears greatest here, when compared to the other time-points, suggesting a possible recovery or excretion of MoS_2 following a prolonged incubation subsequent to exposure.

PCA of NT (red) cells versus T72 (cyan) performed in the HWN range and can be seen in Fig. 5B(ii), in which a degree of separation is achieved, although an overlap of cellular composition is again observed. The differentiating components, represented by PC2 (Fig. 5B(ii)), confirm NT vesicles to be rich in SM lipidic peaks at 2854 cm^{-1} and 3015 cm^{-1}. Cells from the T72 dataset are generally positioned on the negative side of PC2, indicating the presence of lipids from the phosphatidyl family (2844, 2883 and 2981–2991 cm^{-1}). These peaks were also identified in vesicles from both T4 and T24 samples in the range of 2700–3100 cm^{-1}, although a broader distribution of data points within the scatter plot can be seen in cells incubated for 72 h. Similar to the LWN range, no sub-populations or discrete cluster of data points can be detected in T72 (Fig. 5B(ii)), although the overlap with NT cells is still detectable in the HWN range. Furthermore, a decrease in lipid content was detected in cells incubated for 72 h following exposure to MoS_2 (Fig. 1B) and as a result the likelihood of sampling vesicles rich in phosphatidyl lipids or intrinsic SM more balanced. Analysis of variance using a one-way ANOVA revealed reduced levels of significant differences between the mean of NT and T72 datasets, as indicated by a p value of 3.5×10^{-3} and 4.5×10^{-6} for the LWN and HWN regions, respectively.

The evolution of cellular responses over time, following exposure, when compared to untreated cells can be seen in Supplemental Fig. 1 (800–1800 cm^{-1}) and Supplemental Fig. 2 (2700–3100 cm^{-1}). Notably, all differentiating components for analysis preformed in the HWN range of 2700–3100 cm^{-1} are defined according to PC2. This is due to the fact that a high degree of variance is seen in all datasets within this range. In particular, untreated cells (NT) have the highest degree of variance, as can be seen from pre-processed spectra in Supplemental Fig. 3. Interestingly, both T4 and T24 samples exhibit a reduction in spectral variance, indicating a uniform population response following exposure to submicron plates. When THP-1 cells have been allowed a prolonged incubation of 72 h following interaction with MoS_2, the level of variance can be seen to visibly increase in the range of 2700–3100 cm^{-1} (Supplemental Fig. 3). Cellular division is arrested when THP-1 cells have been activated by PMA and therefore, this further indicates the possible recovery of cells following a longer incubation, aiding in our understanding why an overlap of spectral profiles could be seen for NT and T72 datasets.

3.6. Investigation of mixed populations for THP-1 cells incubated for 24 h post exposure

As seen in Fig. 4, point spectra within the T24 dataset appear to have a mixed population of cells, one sub-population being clearly separated from untreated cells based on PC1, while the second has a direct overlap in biochemical composition with NT cells. Therefore, the phenomenon was investigated further by separating the two sub-populations into those of the exposed cells which are clearly differentiated from the untreated calls by PCA ($T24_{T24}$) and those which are grouped with the untreated cells ($T24_{NT}$). $T24_{T24}$ samples are those that were PC1 negative in Fig. 4A(ii) and biochemically different to NT cells, separation between the two datasets being observed. $T24_{NT}$ data points were positioned on the positive side of PC1 and had a clear overlap with NT data points. By segregating the T24 sub-populations, a direct comparison to other time-point datasets can be conducted, to aid in understanding the cellular response following exposure to MoS_2. Data analysis of $T24_{T24}$ versus NT,

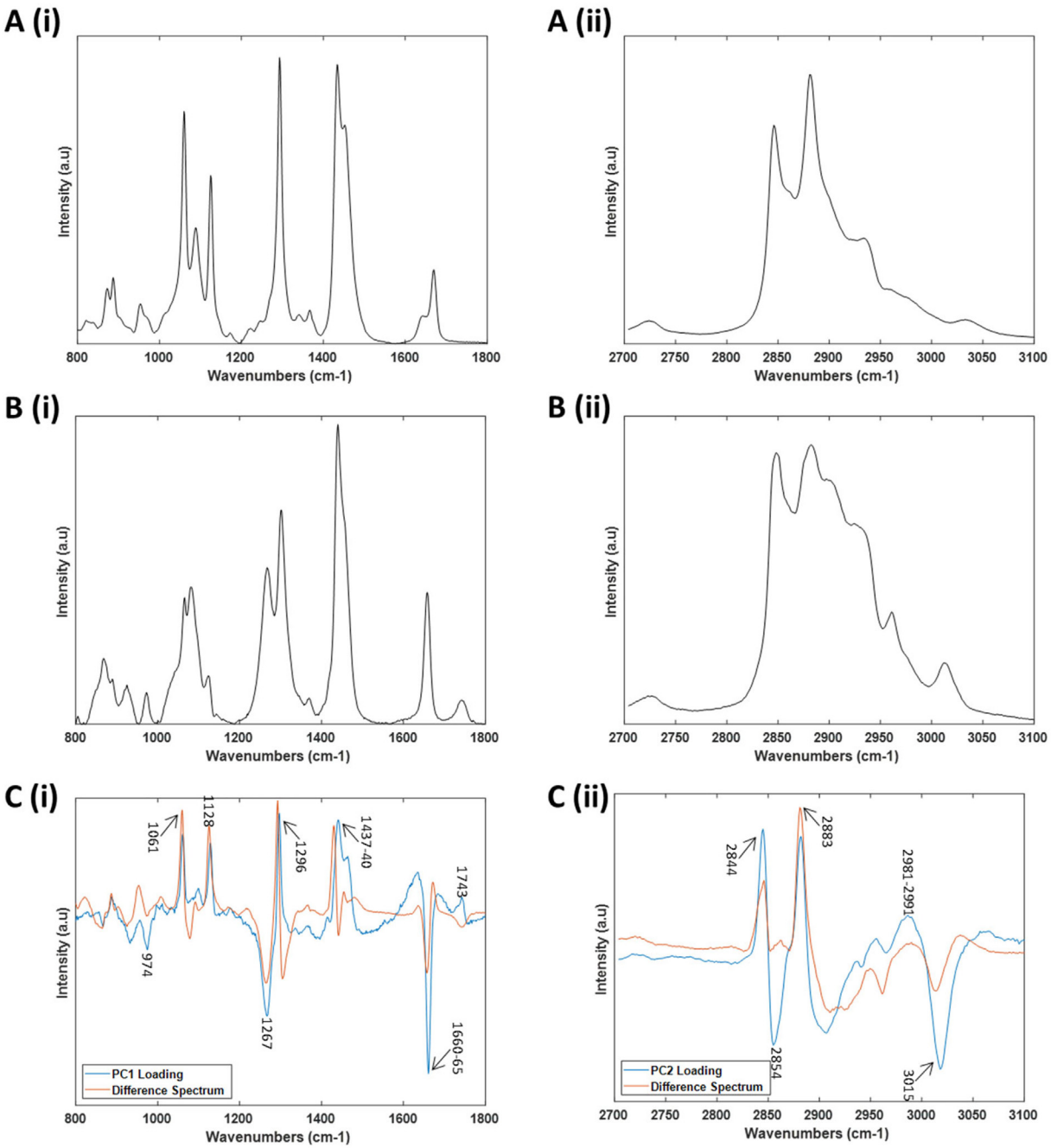

Fig. 3. Identification of lipids detected in PC loadings. Panel A(i) Sphingomyelin standard used to create the difference spectrum in the range 800–1800 cm^{-1}. Panel A (ii) Sphingomyelin standard used to create the difference spectrum in the range 2700–3100 cm^{-1}. Panel B(i) Phosphatidyl standard used to create the difference spectrum in the range 800–1800 cm^{-1}. Panel B(ii) Phosphatidyl standard used to create the difference spectrum in the range 2700–3100 cm^{-1}. Panel C(i) Comparison of PC1 loading (blue) against the difference spectrum (orange) in the range of 800–1800 cm^{-1} (Difference spectrum: Sphingomyelin minus phosphatidyl lipid). Panel C(ii) Comparison of PC2 loading (blue) against the difference spectrum (orange) in the range of 2700–3100 cm^{-1}.

T4 and T72 was conducted and can be seen in Fig. 6. The PCA scatter plot of NT versus $T24_{T24}$ can be seen in Fig. 6A(i), in which clear separation is achieved based on PC1 (Fig. 6A(ii)). A direct correlation with results in Fig. 4A(iii) can be observed, confirming NT to be relatively rich in SM, while $T24_{T24}$ samples are relatively rich in lipids of the phosphatidyl family. If the $T24_{T24}$ samples have a different biochemical composition to the untreated cells, then an overlap with T4 samples would be expected. This is the case and can be seen in Fig. 6B(i), in which no separation is achieved between the T4 and $T24_{T24}$ datasets. Additionally, $T24_{T24}$ samples versus T72 can be seen in the scatter plot Fig. 6C(i), in which partial separation can be observed based on PC1 (Fig. 6C(ii)). PC1 indicates that cells incubated for 72 h post exposure to MoS_2 are more comparable to NT cells (sphingomyelin) than those incubated for either 4 or 24 h (phosphatidyl lipids), further indicating that a prolonged incubation of 72 h in medium results in cellular recovery following exposure to particulate material. Similar trends for $T24_{T24}$ samples were observed in the HWN region and can be seen in Supplemental Fig. 4. A one-way ANOVA revealed significance in cluster separation by a p value ≤0.05 for all test groups within Fig. 6, although higher levels of significance were observed in NT versus T24(T24) ($p = 8.4 \times 10^{-13}$) and T72 versus T24(T24) ($p = 1.1 \times 10^{-5}$) when compared to the higher p value of 2.27×10^{-2} for T4 versus T24(T24).

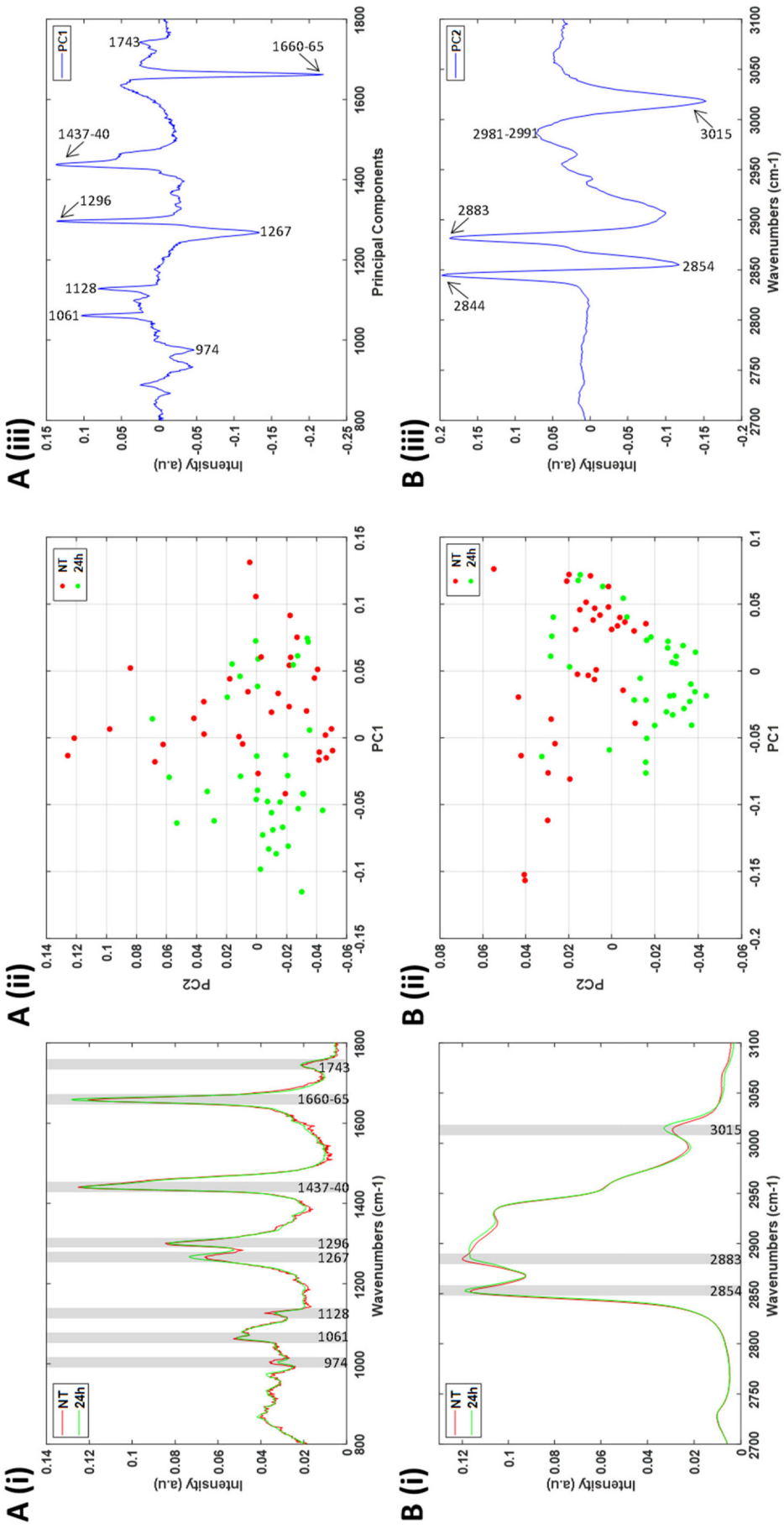

Fig. 4. Principal components analysis to observe differences between untreated THP-1 cells and cell incubated for 24 h following exposure to MoS_2. Panel A(i) pre-processed spectra of NT (red) and 24 h (green) in the range of 800–1800 cm^{-1}. Panel A (ii) PCA scatter plot of Raman spectra from untreated cells (NT, red) and cells incubated for 24 h (green) in the range of 800–1800 cm^{-1}, plotted PC1 versus PC2. Panel A(iii) PC1 loadings demonstrating the spectral differences in the range of 800–1800 cm^{-1}. Panel B(i) pre-processed spectra of NT and 24 h in the range of 2700–3100 cm^{-1}. Panel B(ii) PCA scatter plot of Raman spectra from NT and cells incubated for 24 h in the range of 2700–3100 cm^{-1}, plotted PC1 versus PC2. Panel B(iii) PC2 loadings demonstrating the spectral differences in the range of 2700–3100 cm^{-1}.

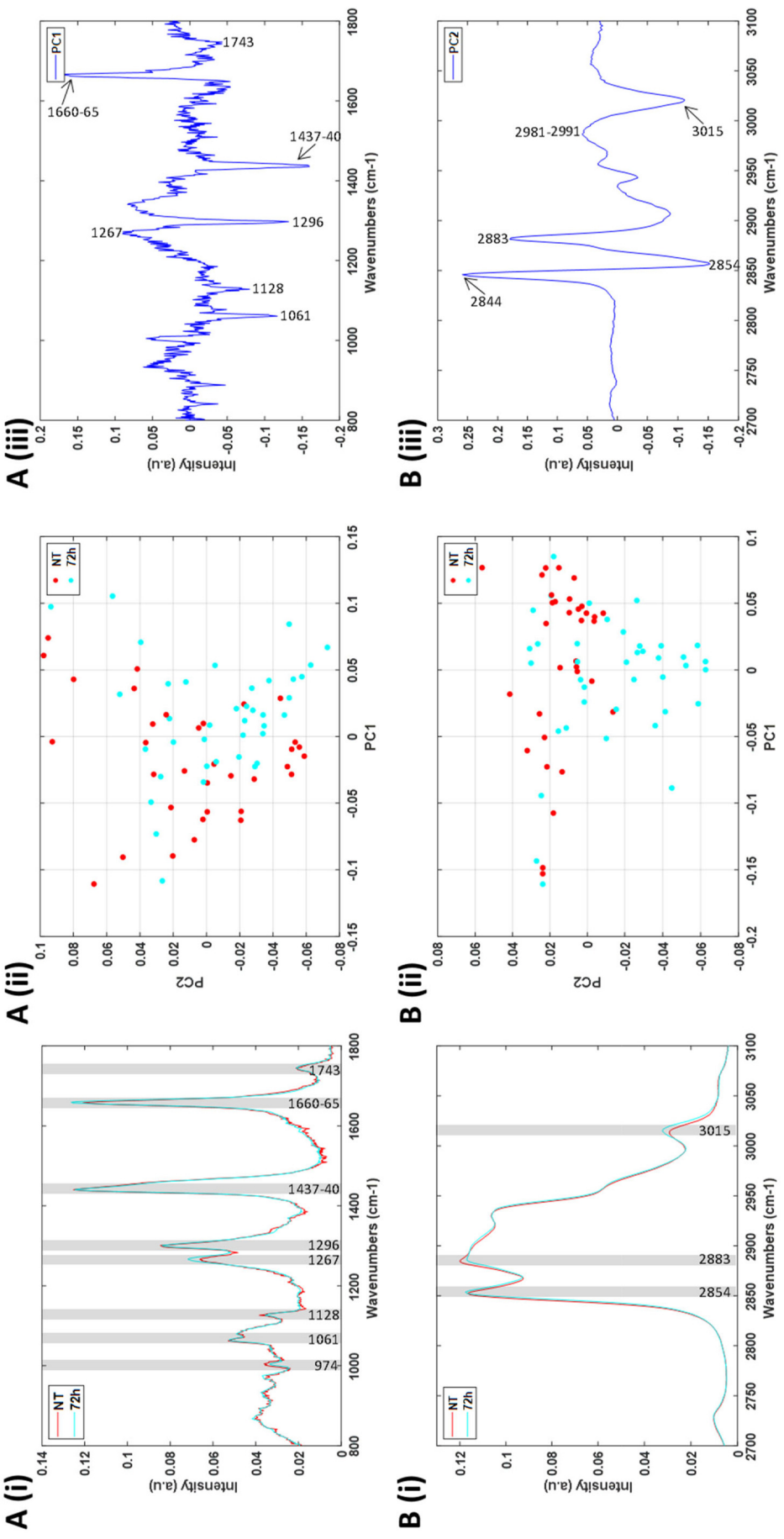

Fig. 5. Principal components analysis to observe differences between untreated THP-1 cells and cell incubated for 72 h following exposure to MoS_2. Panel A(i) pre-processed spectra of NT (red) and 72 h (cyan) in the range of 800–1800 cm^{-1}. Panel A (ii) PCA scatter plot of Raman spectra from untreated cells (NT, red) and cells incubated for 72 h (cyan) in the range of 800–1800 cm^{-1}, plotted PC1 versus PC2. Panel A(iii) PC1 loadings demonstrating the spectral differences in the range of 800–1800 cm^{-1}. Panel B(i) pre-processed spectra of NT and 72 h in the range of 2700–3100 cm^{-1}. Panel B(ii) PCA scatter plot of Raman spectra from NT and cells incubated for 72 h in the range of 2700–3100 cm^{-1}, plotted PC1 versus PC2. Panel B(iii) PC2 loadings demonstrating the spectral differences in the range of 2700–3100 cm^{-1}.

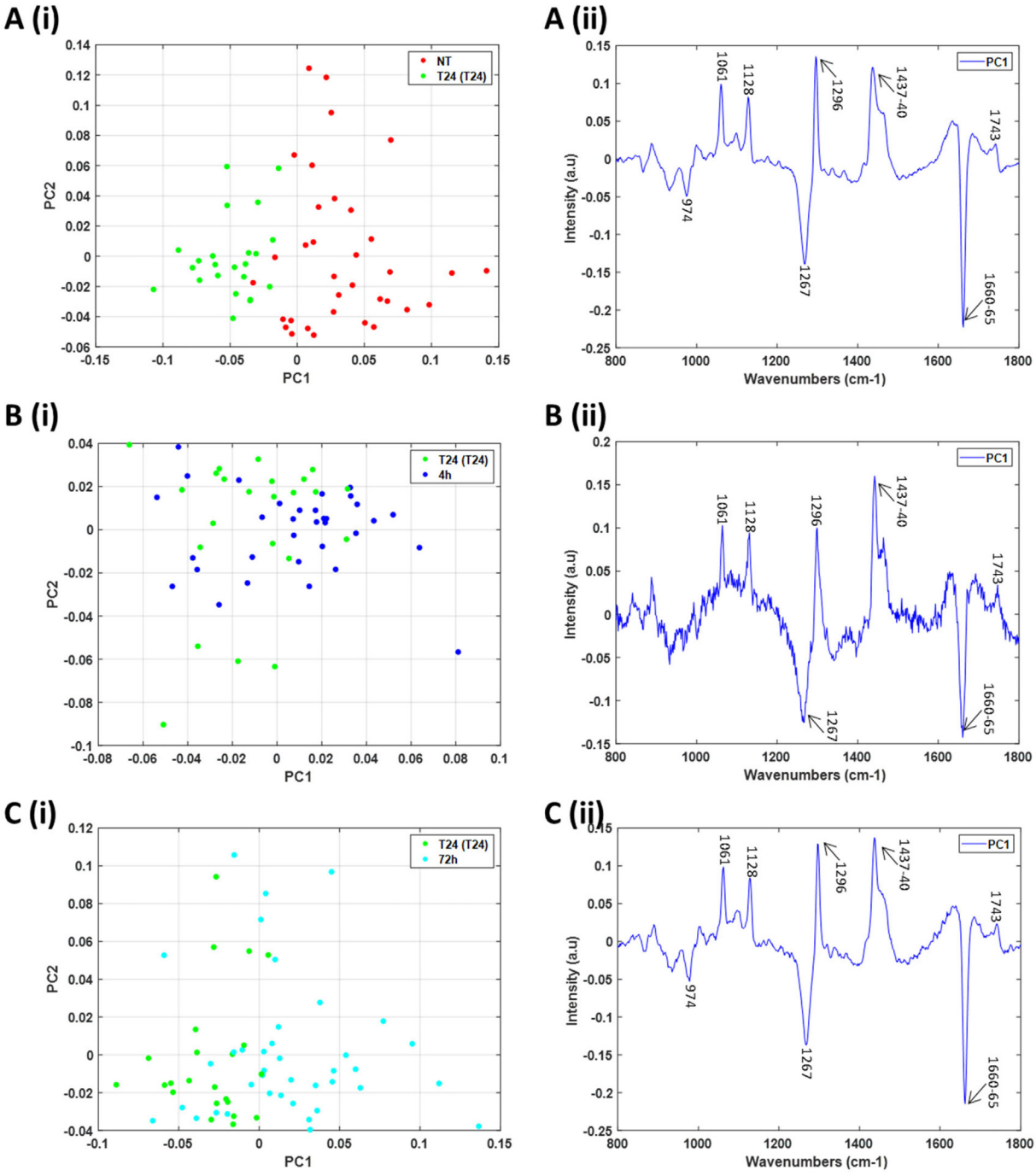

Fig. 6. Principal components analysis to observe differences between $T24_{T24}$ spectra and other time-points. Panel A(i) PCA scatter plot of Raman spectra from NT (red) and $T24_{T24}$ (green), plotted PC1 versus PC2. Panel A(ii) PC1 loadings demonstrating the spectral differences. Panel B(i) PCA scatter plot of Raman spectra 4 h incubation (blue) and $T24_{T24}$ samples (green), plotted PC1 versus PC2. Panel B(ii) PC1 loadings demonstrating the spectral differences. Panel C(i) PCA scatter plot of Raman spectra $T24_{T24}$ samples and (green) and cells incubated for 72 h (cyan), plotted PC1 versus PC2. Panel C(ii) PC1 loadings demonstrating the spectral differences.

PC1 loadings from Fig. 6 have been plotted on a single graph to allow better visualization of biochemical changes over time. Loadings have been offset for clarity. As can be seen in Fig. 7, NT versus $T24_{T24}$ (red) and $T24_{T24}$ versus T72 incubation (cyan) are very similar and further confirm the comparability of NT with point spectra from the T72 dataset. In the comparison of T4 versus $T24_{T24}$ samples, a noisy spectrum is attained, as no clear separation was achieved. Notably, no major differences in biochemical composition can be observed, as all spectra are taken from lipid vesicles within macrophage-like THP-1 cells and a similarity would be expected. Additionally, when comparing the PC1 loadings over time, no major changes in spectral profiles can be observed, although minor alternations in the following peaks can be noted: 931–933, 975, 1098, 1337–1340, 1366 and 1464 cm^{-1}, the majority of which correspond to lipidic constituents.

Based on the findings represented in both Figs. 6 and 7, as expected, the $T24_{T24}$ point spectra are biochemically different to those of NT samples. It was also further established that $T24_{T24}$ samples were similar in composition to cells incubated for 4 h post-exposure (phosphatidyl

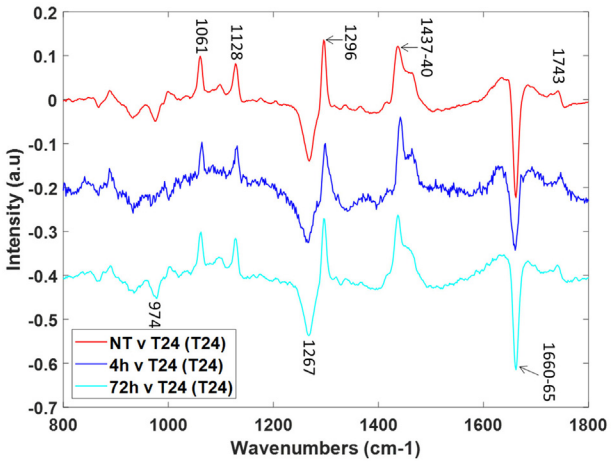

Fig. 7. Comparison of principal component loadings following PCA of $T24_{T24}$ samples versus other time-points. PC1 loading for NT versus $T24_{T24}$ is displayed in red, 4 h versus $T24_{T24}$ is displayed in blue and 72 h versus $T24_{T24}$ is displayed in cyan.

lipids). The next step is to investigate whether the additional sub-population of $T24_{NT}$, which had a clear overlap with NT cells in Fig. 4 A (ii), is indeed similar to untreated cells.

Firstly, PCA was performed on NT cells and the scatter plot can be seen in Fig. 8A(i), in which a broad distribution and high degree of variance can be observed in cells not exposed to particulate material (NT). NT data points were then compared to $T24_{NT}$ samples, resulting in no separation (Fig. 8B(i)). Therefore, this confirms that $T24_{NT}$ have a biochemical composition comparable with NT cells, whose features have been shown to be characterised to be those of SM. Notably, however, $T24_{NT}$ samples appear to have less variance within the dataset when compared to the NT cells. Although the vesicles are similar to those of NT cells, this reduction in biochemical variance may be an in-direct effect as a consequence of exposure to particulate material. Clear separation can be achieved in Fig. 8C(i) when T4 samples are compared to the $T24_{NT}$ data set. Separating components displayed by PC1 in Fig. 8C(ii) show T4 samples are dominated by negative peaks consistent with the phosphatidyl family lipids while $T24_{NT}$ samples contain peaks consistent with previous observations of SM, further confirming the overlap in biochemical composition with NT cells. A one-way ANOVA revealed a p value of 2.6×10^{-1} for NT versus T24(NT) indicating no significance in cluster separation, although significance in separation was achieved for T4 versus T24(NT) ($p = 5.4 \times 10^{-10}$)as indicated by a p value ≤0.05.

$T24_{NT}$ samples were also analysed in the HWN region (Supplemental Fig. 5) in which similar trends were observed showing the robustness of using Raman micro-spectroscopy to obtain the same information from different regions within the spectrum. Figures comparing the T24 sub-populations ($T24_{T24}$ and $T24_{NT}$) against other time-points in the HWN range of 2700–3100 cm^{-1} can be seen in the supplemental information. Similar findings to those reported in the LWN range (800–1800 cm^{-1}) were observed, whereby $T24_{T24}$ samples are seen to have a biochemical composition similar to T4 and T72, while the $T24_{NT}$ datapoints are comparable with NT cells. Additionally, it was further confirmed that the vesicles of $T24_{T24}$ samples are characterised by prominence of members of the phosphatidyl family while those of $T24_{NT}$ samples were comparable to SM, in the spectral range of 2700–3100 cm^{-1}.

3.7. Raman analysis of nuclear point spectra in the spectral range of 800–1800 cm^{-1}

Analysis of point spectra taken from the nuclear region of THP-1 cells was performed in the range of 800–1800 cm^{-1} and can be seen in Fig. 9. The PCA scatter plot of Fig. 9A(i) compares NT (red) and T4 (blue), by which no clear separation can be achieved. A broad distribution of nuclear data points from both datasets can be observed in the scatter plot. The corresponding PC1 loading can be seen in Fig. 9A(ii). No clear differentiating features could be detected between NT and T24 (green) data points (Fig. 9B(i)), and no clear separation is achieved following a longer incubation time. Notably, in contrast to vesicle point spectra, no sub-populations can be observed in the nucleus of cells incubated for 24 h post exposure. PCA of NT (red) nuclear point spectra versus T72 (cyan) can be seen in Fig. 9C(i), in which no distinct separation is achieved, although a considerable amount of T72 samples appear on the negative side of PC1. Additionally, sub-populations in NT data points can be observed with data on both positive and negative sides of PC1. The differentiating spectral features, represented by PC1 (Fig. 9C(ii)), show T72 to be dominated by nucleic acids/DNA/RNA (1324, 1337, 1485 and 1575 cm^{-1}) along with proteins (872, 1003 and 1575 cm^{-1}).

4. Discussion

Prior to the mass production of particulate material for use in both industrial and medical arenas, there is a need to understand their bio-interaction and toxicity with cells. Following the development of material synthesis protocols, the large scale production of material is now a reality, as exemplified by companies such as Talga Resources producing graphene by the tonne in Sweden [43]. Particulate material for industrial applications is fabricated in non-sterile environments in which the risk of contamination is guaranteed. Therefore, the potential for human exposure is high. For example, workers in the manufacturing environment, for consumer and/or at the end of their life cycle. This highlights the need to understand how particulate material interacts with cells and what effect it has prior to human exposure.

Raman micro-spectroscopy has previously been employed to establish material internalisation [20] and to monitor intracellular trafficking [22] of particulate material in-vitro, and its ability to assess the toxicity of nanoparticles in a range of cell types has been demonstrated [44,45]. The distinctive D and G Raman bands have been used to confirm the cellular uptake, degradation and accumulation of both graphene nano flakes and carbon nanotubes [46–49]. Raman micro-spectroscopic mapping was previously employed to obtain a whole cell screen including all regions of the cell to confirm the intracellular localisation of MoS_2 in macrophage-like cells and to explore the degradation of MoS_2 submicron plates, while also obtaining information about the degradation environment [17]. In this study, the main objective was to explore the capability of using Raman micro-spectroscopy as a high content screening tool to monitor the cellular responses and/or nano-bio interaction of immune cells following exposure to MoS_2. To achieve this, the metabolic and sub-cellular response from discrete regions of the cell was targeted, specifically the visually identifiable peri-nuclear vesicles, following exposure to MoS_2 by means of Raman point spectra. Additionally, point spectra obtained from multiple cells allowed a population response to be established. In contrast to the previous Raman mapping study, untreated THP-1 cells were also investigated by Raman point spectra, and monitored as a function of time to determine any biochemical alterations that occur as a result of exposure toMoS_2. Notably, because mapping of individual cells with high spatial resolution is very time consuming, typically only the single spectral window of the fingerprint region is acquired. However, sampling individual points, a significantly broader spectral range can be analysed across multiple cells without unduly increasing the required sampling time.

Before exposure to MoS_2 particulate material, the peri-nuclear regions of differentiated THP-1 cells are seen to be rich in lipidic vesicles. Raman spectral analysis, of both the LWN and HWN regions of the spectrum, shows that the biochemical composition of these vesicles has a strong association with SM, which was identified by comparing PC loadings with pure macromolecule components. SM is a membrane lipid of the sphingolipid (SL) family and is frequently reported as being present

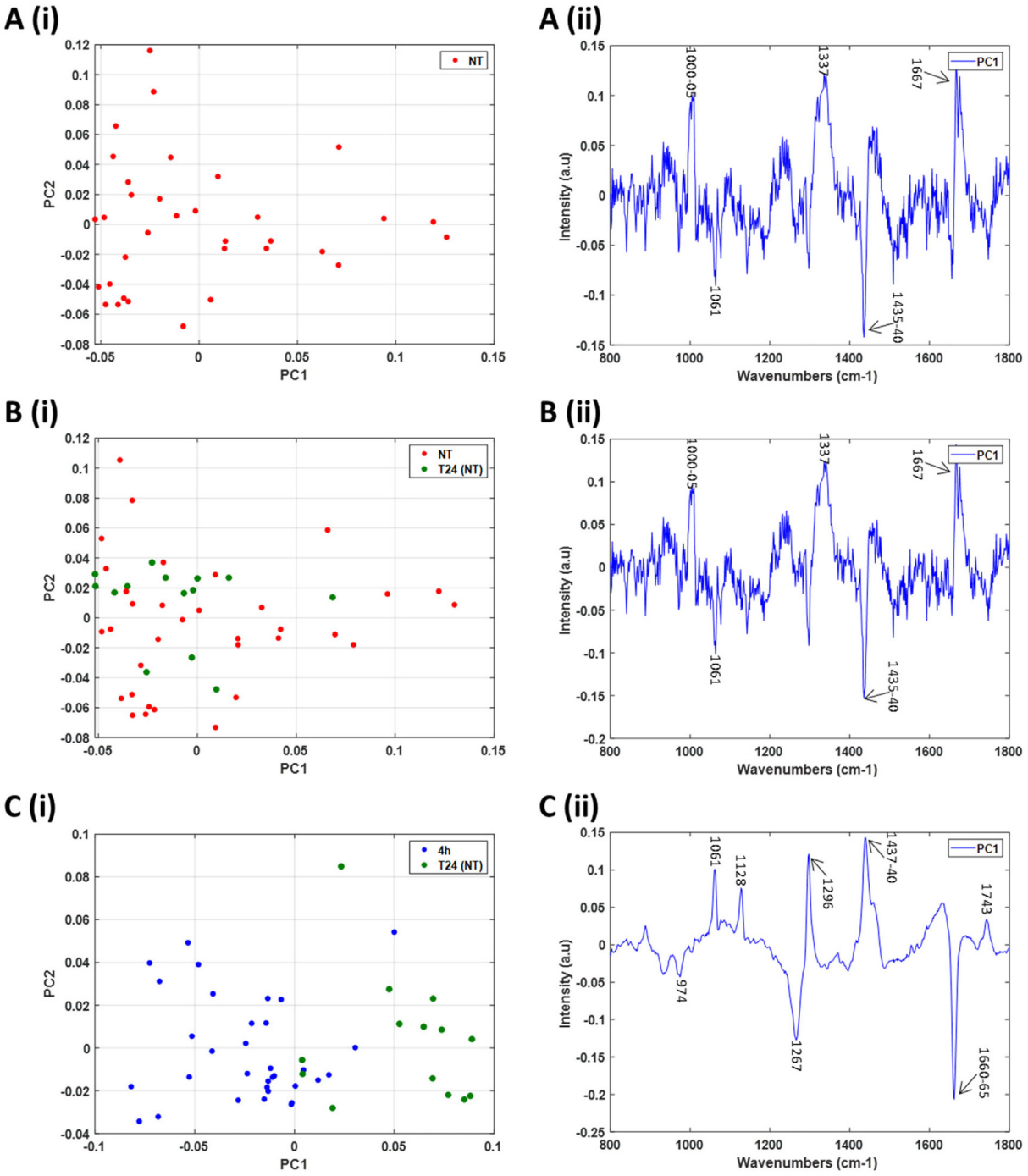

Fig. 8. PCA analysis of $T24_{NT}$ spectral samples with both NT and 4 h incubation. Panel A(i) PCA scatter plot of Raman spectra from NT (red), plotted PC1 versus PC2. Panel A(ii) PC1 loadings demonstrating the spectral differences. Panel B(i) PCA scatter plot of Raman spectra from NT (red) and $T24_{NT}$ samples (dark green), plotted PC1 versus PC2. Panel B(ii) PC1 loadings demonstrating the spectral differences. Panel C(i) PCA scatter plot of Raman spectra from 4 h incubation (blue) and $T24_{NT}$ samples (dark green), plotted PC1 versus PC2. Panel C(ii) PC1 loadings demonstrating the spectral differences.

in both dendritic cells [50] and macrophages [50–52]. SLs are synthesised in the Endoplasmic Reticulum and the Golgi [33] but are accumulated in the cell membrane. Transport from the site of synthesis, in the peri-nuclear region, to the membrane occurs via transport vesicles. SLs self-aggregate at the trans face of the Golgi apparatus by apical budding to form vesicles high in SL concentration, which are subsequently transported to the cytosolic surface [33]. SLs are crucial for cell recruitment and phagocytosis of foreign material and, when inhibited, the clearance of micro-organism/particulate material is greatly affected [50,53]. Therefore, the lipidic vesicles prominent within the peri-nuclear region of untreated THP-1 cells, which can be visualised in Fig. 1A(i) and analysed in Fig. 2(a), confirmed to be rich in SM, may be associated with the generation and transport of SM to the cellular membrane, in which they play a key role in the phagocytotic function of the macrophage cell.

When differentiated THP-1 cells are exposed to MoS_2 for 4 h, to allow internalisation, and incubated for a further 4 h in supplemented medium containing no particulate material, lipidic vesicles of distinctly different biochemical composition were identified in the peri-nuclear region (Fig. 2). PCA of the Raman point spectra in the LWN region

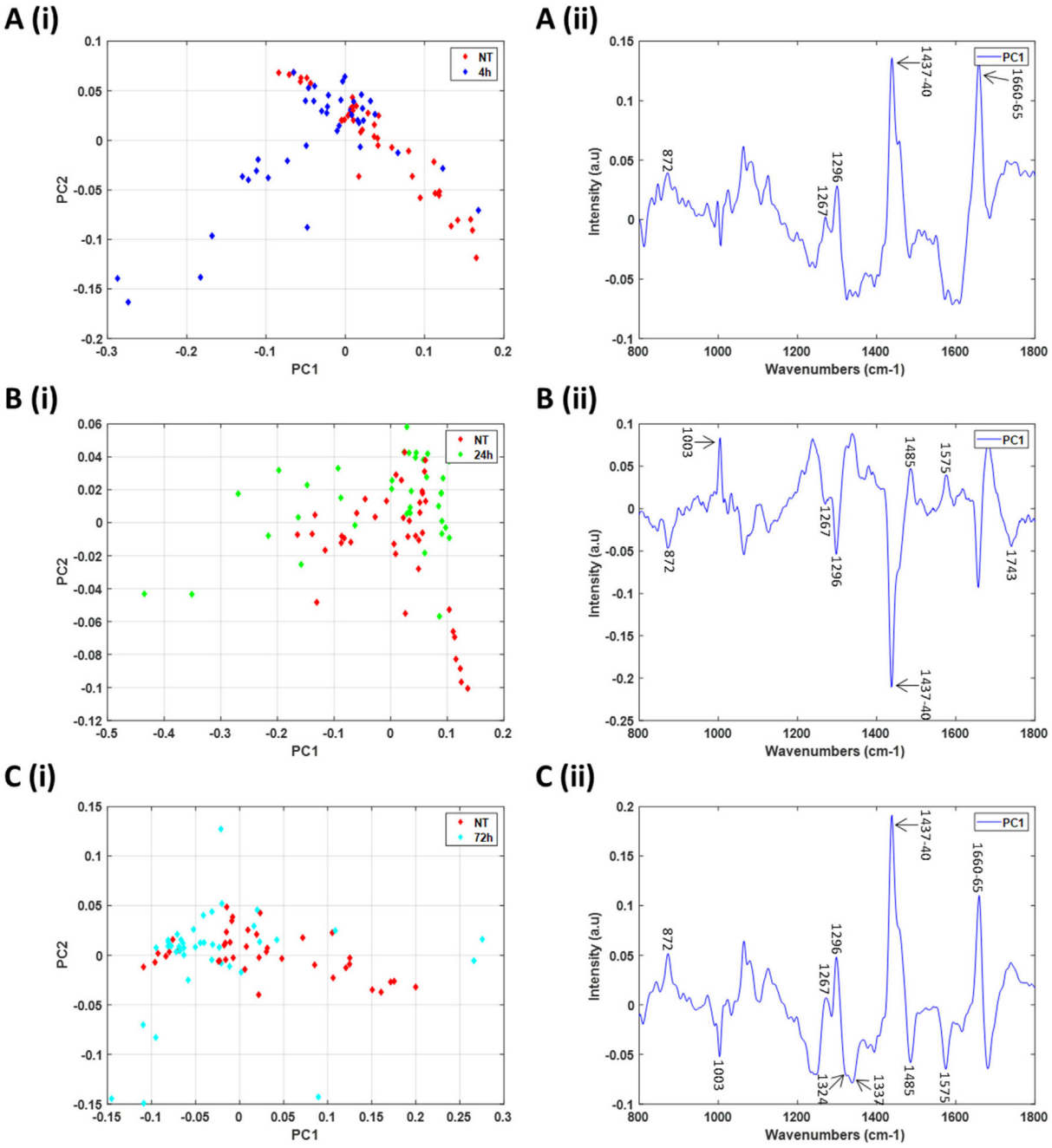

Fig. 9. Principal components analysis of nuclear point spectra in the range of 800–1800 cm^{-1}. Panel A(i) PCA scatter plot of Raman spectra from NT (red) and T4 (blue), plotted PC1 versus PC2. Panel A(ii) corresponding PC1 loading. Panel B(i) PCA scatter plot of Raman spectra from NT and T24 (green), plotted PC1 versus PC2. Panel B(ii) corresponding PC1 loading. Panel C (i) PCA scatter plot of Raman spectra from NT T72 (cyan), plotted PC1 versus PC2. Panel C(ii) corresponding PC1 loading.

(Fig. 2A) indicated that these vesicles had a composition characterised by a prominence of lipids of the phosphatidyl family. This finding was further confirmed by examining the HWN region of 2700–3100 cm^{-1} (Fig. 2B), in which differentiation between NT and T4 was achieved. It should be noted, however, that complete separation in both the LWN and HWN regions is not attained, as evidenced by the overlap in the PCA scatter plot of a few samples, between untreated cells and those exposed to MoS_2. As can be seen from Fig. 1B, in which the lipid content is increased in T4 cells when compared to NT cells, it is possible that the random sampling of the peri-nuclear vesicles was of a mixed population. It is notable that MoS_2, identifiable by its characteristic peaks at ~380 cm^{-1} and 407 cm^{-1}, was clearly present within most, but not all vesicles sampled, at this time point.

Macrophage-like THP-1 cells clearly have the ability to promptly recognise the MoS_2 particulate material and internalise the plates in the short time frame of 4 h [54]. After phagocytosis, the macrophages are in the early stages of processing the foreign material, most likely internalised within phagosomes [15] and this could explain the identification of vesicles with a prominence of phosphatidyl lipids in the T4 dataset (Fig. 2). In Fig. 3, from the library of reference compounds available, the loading is best fitted specifically by the spectrum of phosphatidylserine (PPS), which can be found in abundance on the inner leaflet of the plasma membrane and can be detected on the surface of vesicles as part of the phagocytic pathway [55]. The presence of PPS on the cytosolic surface allows phagosomes to convey a negative charge which is further connected with protein targeting [55]. Likewise,

when phosphatidylcholine (PPC) is hydrolysed to produce phosphatidic acid, an anionic environment is produced causing an increase in the negative charge of phagosomes [55]. Therefore, the presence of phosphatidyl lipids is consistent with a phagosomal processing of the MoS_2 material and possibly aids in phagosome maturation following exposure to MoS_2 material. The prominence of such single membrane vesicles is also consistent with the previously reported TEM observations [17,56]. As a result of exposure to MoS_2 material, an increase in lipid content was detected in T4 cells by the use of Oil Red O staining, which indicates that the probability of sampling a phagosome vesicle rich in phosphatidyl lipids more probable than intrinsic vesicles rich in SM as detected in untreated cells.

When THP-1 cells were incubated for 24 h post-exposure to MoS_2, a similar trend to NT vs T4 was observed, with almost identical differentiating components between vesicles in treated and untreated cells. As the biochemical composition and identification of lipids has already been established for the differentiating components, it can be concluded that the lipidic composition of T24 vesicles is also rich in phosphatidyl lipids. This suggests no drastic cellular changes in the composition of perinuclear vesicles have occurred between the time frame of 4 to 24 h post-exposure to MoS_2. Again, the differentiation between the NT and T24 datasets is not 100%, in either the LWN or HWN regions, and subpopulations could be observed, whereby a small proportion of sampled vesicles had a clear similarity to those of NT (Fig. 4A), although the most prominent observations in the T24 dataset still had phosphatidyl character. This phenomenon was also detected when analysis was completed in the HWN range of 2700–3100 cm^{-1} (Fig. 4B). Notably, this highlights the benefit of using Raman point spectra across multiple cells to obtain a population response as SM sub-populations could not be identified by Raman spectral mapping. As the sampling of the peri-nuclear lipidic vesicles is random, the observation of increased sub-populations of SM dominated vesicles is consistent with a reduced relative population of vesicles of phosphatidyl nature, associated with the phagocytosis.

When cells have been allowed a longer incubation (72 h) in cell culture medium containing no particulate material subsequent to internalisation, molecular differences between sampled vesicles from untreated and treated cells could still be identified. Notably, data points from T72 displayed high variance within the scatter plot (Fig. 5) when compared to other time-points (T4 and T24). Additionally, the shift of T72 data points towards an untreated state can be seen due to ill-defined separation and an overlap between T72 and NT cells in both the LWN and HWN regions. As cells have been exposed to a sub-lethal dose of particulate material and allowed a pro-longed incubation in supplemented media, the macrophage-like cells have had an extended period of time to react, process and recover, following exposure to a foreign threat. Notably, when Oil Red O staining was performed on THP-1 cells, a decrease in internal lipid content could be detected in cells from T72 when compared to T24 cells (Fig. 1B). Therefore, a decrease in vesicles composed of phosphatidyl lipids is suggested and as a result the SM containing vesicles become more prominent and easily detected with Raman micro-spectroscopy.

Notably, when point spectra from 40 cells were analysed following a 24 h incubation, a significant overlap in the PCA scatterplot with those of untreated cells could be observed ($T24_{T24}$ and $T24_{NT}$). A further analysis confirmed that the $T24_{T24}$ subset of datapoints, those that were biochemically different to NT cells, were rich in PPS, while $T24_{NT}$ datapoints, which had a clear overlap in biochemical composition with NT data points were rich in SM. Following a prolonged incubation of 72 h, the spectra of sampled vesicles were more comparable to those of untreated vesicles than those of T4 or T24, and Fig. 1B indicates that the overall lipidic levels have reduced, although not to those of the untreated cells.

The results of the analysis indicate that, in untreated cells, Raman samples the intrinsic vesicles of the macrophages which are rich in SM, a key constituent of the cellular membrane. After exposure, the random selection process of vesicles in the cells samples the relative population of these intrinsically generated, SM transport vesicles, and the PPS dominated vesicles associated with the phagocytosis of the particulate MoS_2. After 4 h, the subcellular environment is dominated by phagosomes, to the extent that is it difficult to image the cells (Fig. 1A (ii)). 24 h after exposure, the subcellular vesicles become better defined, and the PCA scatterplot indicates a more balanced population distribution between SM and PPS dominated lipidic vesicles. Notably, it was previously demonstrated that the degradation profiles of MoS_2 are most prominent at this timepoint [17], and that a significant proportion of the lipidic content of the culture has been externalised, potentially by exocytosis of degraded material. At 72 h after exposure, the cell population has largely returned to normal, although non-degraded MoS_2 was previously detected in cells at this timepoint. The vesicular environment surrounding non-degraded material was further differentiated, and identified as predominantly lysozyme, and it was suggested that the LPS on the surface of particulate material causes a reduction in the activity of this enzyme [17,57].

Macrophage like cells have been exposed to a pre-determined sub-lethal dose of industrial grade MoS_2 and previously no signs of nuclear stress, DNA damage or genotoxicity was observed by laser scanning confocal microscopy and therefore the likelihood of nuclear damage is expected to be low. Nevertheless, nuclear point spectra were also included in the experimental design to investigate whether any biochemical changes have occurred as a consequence of exposure. As seen in Fig. 9, no distinct separation could be achieved for any of the incubation time-points. Notably, data points from T72 are mainly positioned on the negative side of PC1 although an overlap with NT cells is observed. Nuclear point spectra have been used to assess the toxicology of particulate material for indications of DNA damage, apoptosis and/or necrosis [58] although these trends could not be observed in THP-1 cells following exposure to MoS_2.

The study demonstrates the advantage of analysis based on multiple Raman point spectra, such that a larger proportion of the population can be examined when compared to high resolution spectral maps. The benefit of obtaining Raman point spectra from discrete sub-cellular regions from multiple cells over time allows the identification of this trend in biochemical alterations between untreated cells and those exposed to MoS_2 to be identified. Typically, the wavenumber range of 400–1800 cm^{-1} is usually recorded, as this fingerprint region contains a vast amount of information. For this study, a larger wavenumber range was recorded to incorporate both the LWN and HWN regions, allowing verification of biochemical macromolecules from two regions within the same spectra for each cell. In this investigation, the HWN region was utilised as a confirmation tool, although it showcases the advantages of using HWN region as an approach for a reliable, fast and effective screening method, particular when lipids play a prominent role in the cellular response.

Additionally, this study has confirmed the robustness of using Raman micro-spectroscopy in the field of micro/nanomaterial screening as the characteristics of point spectra from multiple cells in this study were comparable to lipids identified when previously performing Raman spectral maps. Notably, intrinsic SM vesicles were not detectable in macrophage-like cells following exposure to MoS_2 (4, 24 or 72 h) by means of whole-cell mapping and therefore this further highlights the limitations of Raman spectral mapping to monitor cellular responses. The benefits of using Raman point spectra to monitor cellular responses over time and to determine a population response has been highlighted within this study, while Raman spectral mapping proved more effective for demonstrating the localisation and trafficking of MoS_2 within single cells while also providing the local environment in which it was encompassed.

5. Conclusion

In conclusion, confocal Raman micro-spectroscopy has demonstrated to be a powerful tool for profiling the cellular response of

macrophage-like immune cells following exposure to industrial grade MoS_2. Changes in biochemical composition of vesicles positioned in the peri-nuclear cloud could be assessed and monitored as a function of time, to provide detailed information to aid in understanding cellular responses. Biochemical changes on a sub-cellular level were detected as a result of exposure to particulate material. The biochemical composition of vesicles present in untreated cells had a high prominence of the membrane lipid sphingomyelin. When macrophage-like cells have been exposed to MoS_2, vesicles with a different biochemical composition could be detected. *V*esicles from cells incubated for 4, 24 or 72 h following exposure were associated with an environment rich in phosphatidyl lipids. Additionally, vesicles with a high prominence of sphingomyelin and phosphatidyl lipids could be detected in cells incubated for 24 h. Following a prolonged incubation of 72 h, vesicles are still distinguishable from those of untreated cells although a recovery to the normal state is suggested. Notably, no nuclear stress or DNA alterations could be observed following a 4, 24 or 72 h incubation, as would be expected for a sub-lethal dose. The benefit of using a label-free and non-destructive technique allows the application to be transferrable and adaptable for different cell types to carry out screening for a wide range of micro/nanoparticles.

CRediT authorship contribution statement

Author	Contribution
Caroline Moore	Conceptualization, Methodology, Software, Investigation, Writing, Visualization
Andrew Harvey	Methodology, Investigation, Writing-Review and editing
Jonathan N. Coleman	Methodology, Writing-Review and editing,
Hugh J. Byrne	Conceptualization, Writing-Review and editing, Supervision
Jennifer McIntyre	Conceptualization, Writing-Review and editing, Supervision

Declaration of competing interest

The authors declare that they have no known competing financial interests or personal relationships that could have appeared to influence the work reported in this paper.

Acknowledgements

CM was supported by the Dublin Institute of Technology Fiosraigh Scholarship scheme.

Appendix A. Supplementary data

Supplementary data to this article can be found online at https://doi.org/10.1016/j.saa.2020.118916.

References

[1] R.P. Feynman, There's plenty of room at the bottom, Eng. Sci. 23 (1960) 22–36http://resolver.caltech.edu/CaltechES:23.5.1960Bottom. (Accessed 19 September 2017).
[2] K.S. Novoselov, A.K. Geim, S.V. Morozov, D. Jiang, Y. Zhang, S.V. Dubonos, I.V. Grigorieva, A.A. Firsov, Electric field effect in atomically thin carbon films, Science (80-.) 306 (2004) 666–669, https://doi.org/10.1126/science.1102896.
[3] T. Das, B.K. Sharma, A.K. Katiyar, J.H. Ahn, Graphene-based flexible and wearable electronics, J. Semicond. 39 (2018)https://doi.org/10.1088/1674-4926/39/1/011007.
[4] H. Huang, S. Su, N. Wu, H. Wan, S. Wan, H. Bi, L. Sun, Graphene-based sensors for human health monitoring, Front. Chem. 7 (2019)https://doi.org/10.3389/fchem.2019.00399.
[5] J. Liu, L. Cui, D. Losic, Graphene and graphene oxide as new nanocarriers for drug delivery applications, Acta Biomater. 9 (2013) 9243–9257, https://doi.org/10.1016/j.actbio.2013.08.016.
[6] J.N. Coleman, M. Lotya, A. O'Neill, S.D. Bergin, P.J. King, U. Khan, K. Young, A. Gaucher, S. De, R.J. Smith, I.V. Shvets, S.K. Arora, G. Stanton, H.-Y. Kim, K. Lee, G.T. Kim, G.S. Duesberg, T. Hallam, J.J. Boland, J.J. Wang, J.F. Donegan, J.C. Grunlan, G. Moriarty, A. Shmeliov, R.J. Nicholls, J.M. Perkins, E.M. Grieveson, K. Theuwissen, D.W. McComb, P.D. Nellist, V. Nicolosi, Two-dimensional nanosheets produced by liquid exfoliation of layered materials, Science 331 (2011) 568–571, https://doi.org/10.1126/science.1194975.
[7] E. Varrla, C. Backes, K.R. Paton, A. Harvey, Z. Gholamvand, J. McCauley, J.N. Coleman, Large-scale production of size-controlled MoS_2 nanosheets by shear exfoliation, Chem. Mater. 27 (2015) 1129–1139, https://doi.org/10.1021/cm5044864.
[8] K.F. Mak, C. Lee, J. Hone, J. Shan, T.F. Heinz, Atomically thin MoS2: a new direct-gap semiconductor, Phys. Rev. Lett. 105 (2010) 2–5, https://doi.org/10.1103/PhysRevLett.105.136805.
[9] X. Li, H. Zhu, Two-dimensional MoS2: properties, preparation, and applications, J. Mater. 1 (2015) 33–44, https://doi.org/10.1016/j.jmat.2015.03.003.
[10] R. Ganatra, Q. Zhang, Few-layer MoS2: a promising layered semiconductor, ACS Nano 8 (2014) 4074–4099, https://doi.org/10.1021/nn405938z.
[11] P. Wick, A.E. Louw-Gaume, M. Kucki, H.F. Krug, K. Kostarelos, B. Fadeel, K.A. Dawson, A. Salvati, E. Vázquez, L. Ballerini, M. Tretiach, F. Benfenati, E. Flahaut, L. Gauthier, M. Prato, A. Bianco, Classification framework for graphene-based materials, Angew. Chemie Int. Ed. 53 (2014) 7714–7718, https://doi.org/10.1002/anie.201403335.
[12] A. Bianco, H.M. Cheng, T. Enoki, Y. Gogotsi, R.H. Hurt, N. Koratkar, T. Kyotani, M. Monthioux, C.R. Park, J.M.D. Tascon, J. Zhang, All in the graphene family - a recommended nomenclature for two-dimensional carbon materials, Carbon N. Y. 65 (2013) 1–6, https://doi.org/10.1016/j.carbon.2013.08.038.
[13] ISO - ISO/TS 80004-2:2015 - nanotechnologies — Vocabulary — Part 2: Nano-objects, (n.d.). https://www.iso.org/standard/54440.html (accessed December 5, 2019).
[14] J. Yang, L. Zhang, C. Yu, X.F. Yang, H. Wang, Monocyte and macrophage differentiation: circulation inflammatory monocyte as biomarker for inflammatory diseases, Biomark. Res. 2 (2014)https://doi.org/10.1186/2050-7771-2-1.
[15] S. Gordon, The macrophage: past, present and future, Eur. J. Immunol. 37 (2007) S9–S17, https://doi.org/10.1002/eji.200737638.
[16] C. Moore, D. Movia, R.J. Smith, D. Hanlon, F. Lebre, E.C. Lavelle, H.J. Byrne, J.N. Coleman, Y. Volkov, J. McIntyre, Industrial grade 2D molybdenum disulphide (MoS_2): an *in vitro* exploration of the impact on cellular uptake, cytotoxicity, and inflammation, 2D Mater. 4 (2017) 025065, https://doi.org/10.1088/2053-1583/aa673f.
[17] C. Moore, A. Harvey, J.N. Coleman, H. Byrne, J. McIntyre, In-vitro localisation and degradation of few-layer MoS2; submicrometric plates in human macrophage-like cells: a label free Raman micro-spectroscopic study, 2D Mater. (2019)https://doi.org/10.1088/2053-1583/ab5d98.
[18] R. Kurapati, L. Muzi, A.P.R. de Garibay, J. Russier, D. Voiry, I.A. Vacchi, M. Chhowalla, A. Bianco, Enzymatic biodegradability of pristine and functionalized transition metal dichalcogenide MoS_2 nanosheets, Adv. Funct. Mater. 27 (2017) 1605176, https://doi.org/10.1002/adfm.201605176.
[19] K.M. Davis, J.N. Weiser, Modifications to the peptidoglycan backbone help bacteria to establish infection, Infect. Immun. 79 (2011) 562–570, https://doi.org/10.1128/IAI.00651-10.
[20] J. Dorney, F. Bonnier, A. Garcia, A. Casey, G. Chambers, H.J. Byrne, Identifying and localizing intracellular nanoparticles using Raman spectroscopy, Analyst. 137 (2012) 1111, https://doi.org/10.1039/c2an15977e.
[21] M.E. Keating, F. Bonnier, H.J. Byrne, Spectral cross-correlation as a supervised approach for the analysis of complex Raman datasets: the case of nanoparticles in biological cells, Analyst. 137 (2012) 5792, https://doi.org/10.1039/c2an36169h.
[22] E. Efeoglu, M. Keating, J. McIntyre, A. Casey, H.J. Byrne, Determination of nanoparticle localisation within subcellular organelles in vitro using Raman spectroscopy, Anal. Methods 7 (2015) 10000–10017, https://doi.org/10.1039/C5AY02661J.
[23] H.J. Butler, L. Ashton, B. Bird, G. Cinque, K. Curtis, J. Dorney, K. Esmonde-White, N.J. Fullwood, B. Gardner, P.L. Martin-Hirsch, M.J. Walsh, M.R. McAinsh, N. Stone, F.L. Martin, Using Raman spectroscopy to characterize biological materials, Nat. Protoc. 11 (2016) 664–687, https://doi.org/10.1038/nprot.2016.036.
[24] C. Backes, B.M. Szydłowska, A. Harvey, S. Yuan, V. Vega-Mayoral, B.R. Davies, P.L. Zhao, D. Hanlon, E.J.G. Santos, M.I. Katsnelson, W.J. Blau, C. Gadermaier, J.N. Coleman, Production of highly monolayer enriched dispersions of liquid-exfoliated nanosheets by liquid cascade centrifugation, ACS Nano 10 (2016) 1589–1601, https://doi.org/10.1021/acsnano.5b07228.
[25] R.J. Smith, P.J. King, M. Lotya, C. Wirtz, U. Khan, S. De, A. O'Neill, G.S. Duesberg, J.C. Grunlan, G. Moriarty, J. Chen, J.Z. Wang, A.I. Minett, V. Nicolosi, J.N. Coleman, Large-scale exfoliation of inorganic layered compounds in aqueous surfactant solutions, Adv. Mater. 23 (2011) 3944−+, https://doi.org/10.1002/adma.201102584.
[26] C. Backes, R.J. Smith, N. McEvoy, N.C. Berner, D. McCloskey, H.C. Nerl, A. O'Neill, P.J. King, T. Higgins, D. Hanlon, N. Scheuschner, J. Maultzsch, L. Houben, G.S. Duesberg, J.F. Donegan, V. Nicolosi, J.N. Coleman, Edge and confinement effects allow in situ measurement of size and thickness of liquid-exfoliated nanosheets, Nat. Commun. 5 (2014)https://doi.org/10.1038/ncomms5576.
[27] M. Daigneault, J.A. Preston, H.M. Marriott, M.K.B. Whyte, D.H. Dockrell, The identification of markers of macrophage differentiation in PMA-stimulated THP-1 cells and monocyte-derived macrophages, PLoS One 5 (2010), e8668, https://doi.org/10.1371/journal.pone.0008668.
[28] F. Draux, C. Gobinet, J. Sulé-Suso, A. Trussardi, M. Manfait, P. Jeannesson, G.D. Sockalingum, Raman spectral imaging of single cancer cells: probing the impact of sample fixation methods, Anal. Bioanal. Chem. Springer 2010, pp. 2727–2737, https://doi.org/10.1007/s00216-010-3759-8.

[29] L.T. Kerr, H.J. Byrne, B.M. Hennelly, Optimal choice of sample substrate and laser wavelength for Raman spectroscopic analysis of biological specimen, Anal. Methods 7 (2015) 5041–5052, https://doi.org/10.1039/C5AY00327J.
[30] L.T. Kerr, B.M. Hennelly, A multivariate statistical investigation of background subtraction algorithms for Raman spectra of cytology samples recorded on glass slides, Chemom. Intell. Lab. Syst. 158 (2016) 61–68, https://doi.org/10.1016/j.chemolab.2016.08.012.
[31] Z. Farhane, F. Bonnier, A. Casey, A. Maguire, L. O'Neill, H.J. Byrne, Cellular discrimination using in vitro Raman micro spectroscopy: the role of the nucleolus, Analyst. 140 (2015) 5908–5919, https://doi.org/10.1039/C5AN01157D.
[32] T. Dellibovi-Ragheb, N. Altan-Bonnet, Cloud storage for endosomes, EMBO J. 35 (2016) 1724–1725, https://doi.org/10.15252/embj.201695080.
[33] G. Van Meer, Q. Lisman, Sphingolipid transport: rafts and translocators, J. Biol. Chem. 277 (2002) 25855–25858, https://doi.org/10.1074/jbc.R200010200.
[34] M. Placidi, M. Dimitrievska, V. Izquierdo-Roca, X. Fontané, A. Castellanos-Gomez, A. Pérez-Tomás, N. Mestres, M. Espindola-Rodriguez, S. López-Marino, M. Neuschitzer, V. Bermudez, A. Yaremko, A. Pérez-Rodríguez, Multiwavelength excitation Raman scattering analysis of bulk and two-dimensional MoS_2: vibrational properties of atomically thin MoS_2 layers, 2D Mater. 2 (2015) 035006, https://doi.org/10.1088/2053-1583/2/3/035006.
[35] M. Ye, D. Winslow, D. Zhang, R. Pandey, Y. Yap, M. Ye, D. Winslow, D. Zhang, R. Pandey, Y.K. Yap, Recent advancement on the optical properties of two-dimensional molybdenum disulfide (MoS2) thin films, Photonics. 2 (2015) 288–307, https://doi.org/10.3390/photonics2010288.
[36] Z. Movasaghi, S. Rehman, I.U. Rehman, Raman spectroscopy of biological tissues, Appl. Spectrosc. Rev. 42 (2007) 493–541, https://doi.org/10.1080/05704920701551530.
[37] J.R. Beattie, S.E.J. Bell, B.W. Moss, A critical evaluation of Raman spectroscopy for the analysis of lipids: fatty acid methyl esters, Lipids. 39 (2004) 407–419, https://doi.org/10.1007/s11745-004-1245-z.
[38] L.J. den Hartigh, J.E. Connolly-Rohrbach, S. Fore, T.R. Huser, J.C. Rutledge, Fatty acids from very low-density lipoprotein lipolysis products induce lipid droplet accumulation in human monocytes, J. Immunol. 184 (2010) 3927–3936, https://doi.org/10.4049/jimmunol.0903475.
[39] H. Wu, J.V. Volponi, A.E. Oliver, A.N. Parikh, B.A. Simmons, S. Singh, In vivo lipidomics using single-cell Raman spectroscopy, Proc. Natl. Acad. Sci. U. S. A. 108 (2011) 3809–3814, https://doi.org/10.1073/pnas.1009043108.
[40] C. Zhang, Y. Wang, F. Wang, Z. Wang, Y. Lu, Y. Xu, K. Wang, H. Shen, P. Yang, S. Li, X. Qin, H. Yu, Quantitative profiling of glycerophospholipids during mouse and human macrophage differentiation using targeted mass spectrometry, Sci. Rep. 7 (2017) 412, https://doi.org/10.1038/s41598-017-00341-2.
[41] J.M. Berg, J.L. Tymoczko, L. Stryer, Lipids and cell membranes, Biochemistry, 5th ed. W H Freeman, 2002https://www.ncbi.nlm.nih.gov/books/NBK22361/. (Accessed 30 May 2019).
[42] V. Caprettini, J.-A. Huang, F. Moia, A. Jacassi, C.A. Gonano, N. Maccaferri, R. Capozza, M. Dipalo, F. De Angelis, Enhanced Raman investigation of cell membrane and intracellular compounds by 3D Plasmonic Nanoelectrode arrays, Adv. Sci. 5 (2018) 1800560, https://doi.org/10.1002/advs.201800560.
[43] Talga Resources, (n.d.). http://www.talgaresources.com/IRM/content/default.aspx (accessed January 23, 2020).
[44] E. Efeoglu, A. Casey, H.J. Byrne, In vitro monitoring of time and dose dependent cytotoxicity of aminated nanoparticles using Raman spectroscopy, Analyst. 141 (2016) 5417–5431, https://doi.org/10.1039/c6an01199c.
[45] E. Efeoglu, A. Casey, H.J. Byrne, Determination of spectral markers of cytotoxicity and genotoxicity using in vitro Raman microspectroscopy: cellular responses to polyamidoamine dendrimer exposure, Analyst. 142 (2017) 3848–3856, https://doi.org/10.1039/c7an00969k.
[46] F. Alnasser, V. Castagnola, L. Boselli, M. Esquivel-Gaon, E. Efeoglu, J. McIntyre, H.J. Byrne, K.A. Dawson, Graphene nanoflake uptake mediated by scavenger receptors, Nano Lett. 19 (2019) 1260–1268, https://doi.org/10.1021/acs.nanolett.8b04820.
[47] J. Bin Wu, M.L. Lin, X. Cong, H.N. Liu, P.H. Tan, Raman spectroscopy of graphene-based materials and its applications in related devices, Chem. Soc. Rev. 47 (2018) 1822–1873, https://doi.org/10.1039/c6cs00915h.
[48] J. McIntyre, N.K. Verma, R.J. Smith, C. Moore, H. Nerl, N. McEvoy, N. Berner, I. McGovern, U. Khan, P. Lyons, L. O'Neill, V. Nicolosi, G.S. Duesberg, H.J. Byrne, J. Coleman, Y. Volkov, A comparison of catabolic pathways induced in primary macrophages by pristine single walled carbon nanotubes and pristine graphene, RSC Adv. 6 (2016) 65299–65310, https://doi.org/10.1039/C6RA02476A.
[49] V.E. Kagan, N.V. Konduru, W. Feng, B.L. Allen, J. Conroy, Y. Volkov, I.I. Vlasova, N.A. Belikova, N. Yanamala, A. Kapralov, Y.Y. Tyurina, J. Shi, E.R. Kisin, A.R. Murray, J. Franks, D. Stolz, P. Gou, J. Klein-Seetharaman, B. Fadeel, A. Star, A.A. Shvedova, Carbon nanotubes degraded by neutrophil myeloperoxidase induce less pulmonary inflammation, Nat. Nanotechnol. 5 (2010) 354–359, https://doi.org/10.1038/nnano.2010.44.
[50] T. Lallemand, M. Rouahi, A. Swiader, M.H. Grazide, N. Geoffre, P. Alayrac, E. Recazens, A. Coste, R. Salvayre, A. Nègre-Salvayre, N. Augé, NSMase2 (type 2-neutral sphingomyelinase) deficiency or inhibition by GW4869 reduces inflammation and atherosclerosis in Apoe −/− mice, Arterioscler. Thromb. Vasc. Biol. 38 (2018) 1479–1492, https://doi.org/10.1161/ATVBAHA.118.311208.
[51] K. Zhou, T. Blom, Trafficking and functions of bioactive sphingolipids: lessons from cells and model membranes, Lipid Insights. 2015 (2015) 11–20, https://doi.org/10.4137/LPI.S31615.
[52] T.C. Kunz, V. Kozjak-Pavlovic, Diverse facets of sphingolipid involvement in bacterial infections, Front. Cell Dev. Biol. 7 (2019) 203, https://doi.org/10.3389/fcell.2019.00203.
[53] F.G. Tafesse, A. Rashidfarrokhi, F.I. Schmidt, E. Freinkman, S. Dougan, M. Dougan, A. Esteban, T. Maruyama, K. Strijbis, H.L. Ploegh, Disruption of sphingolipid biosynthesis blocks phagocytosis of Candida albicans, PLoS Pathog. 11 (2015), e1005188, https://doi.org/10.1371/journal.ppat.1005188.
[54] C. Moore, D. Movia, R.J. Smith, D. Hanlon, F. Lebre, E.C. Lavelle, H.J. Byrne, J.N. Coleman, Y. Volkov, J. McIntyre, Industrial grade 2D molybdenum disulphide (MoS_2): an *in vitro* exploration of the impact on cellular uptake, cytotoxicity, and inflammation, 2D Mater. 4 (2017) 025065, https://doi.org/10.1088/2053-1583/aa673f.
[55] B.E. Steinberg, S. Grinstein, Pathogen destruction versus intracellular survival: the role of lipids as phagosomal fate determinants, J. Clin. Invest. 118 (2008) 2002–2011, https://doi.org/10.1172/JCI35433.
[56] D.J. Klionsky, E.L. Eskelinen, V. Deretic, Autophagosomes, phagosomes, autolysosomes, phagolysosomes, autophagolysosomes… Wait, I'm confused, Autophagy. 10 (2014) 549–551, https://doi.org/10.4161/auto.28448.
[57] J. Lukasiewicz, C. Lugowski, Editorial: O-specific polysaccharide confers lysozyme resistance to extraintestinal pathogenic Escherichia coli, Virulence. 9 (2018) 919–922, https://doi.org/10.1080/21505594.2018.1460188.
[58] E. Efeoglu, M.A. Maher, A. Casey, H.J. Byrne, Toxicological assessment of nanomaterials: the role of in vitro Raman microspectroscopic analysis, Anal. Bioanal. Chem. 410 (2018) 1631–1646, https://doi.org/10.1007/s00216-017-0812-x.